American Mineralogist, Volume 97, pages 816–827, 2012

Determination of Mn valence states in mixed-valent manganates by XANES spectroscopy

Alain Manceau,[1,*] Matthew A. Marcus,[2] and Sylvain Grangeon[1,†]

[1]ISTerre, CNRS and Université de Grenoble 1, F-38041 Grenoble Cedex 9, France
[2]Advanced Light Source, Lawrence Berkeley National Laboratory, One Cyclotron Road, Berkeley, California 94720, U.S.A.

Abstract

The valence states of Mn in mixed-valent layer and tunnel structure manganese dioxides (MnO_2), usually referred to as phyllomanganates and tectomanganates, can be measured by X-ray absorption near-edge structure (XANES) spectroscopy with a precision and accuracy that are difficult to estimate owing to the paucity of well-characterized standards. A compilation of the Mn *K*-edge XANES spectra of most naturally occurring manganates, synthetic analogs of known structure and chemical composition, and pure-valence phase species is presented and made available as an open source. We intend this compilation to serve as a basis for the spectroscopic determination of the fractions of the Mn 2+, 3+, and 4+ valences in mixed-valent manganates and phase mixtures. The XANES derivatives of tectomanganates and phyllomanganates with no or little Mn^{3+} in the MnO_2 layer exhibit intensities, shapes, and relative energy positions of the main features characteristics of a particular valence composition. For these compounds, valence fractions can be derived using linear combination fitting analysis. Best quantitative results are obtained when the unknown spectrum is fit to a weighted sum of all reference spectra in the database with the fractions of species constrained to be non-negative (Combo method). The accuracy of the average valence is estimated to 0.04 v.u. in the range of 3+ to 4+, and decreases when the proportion of divalent Mn is higher than 15%. The accuracy of the method is also lower in (layer Mn^{3+}, Mn^{4+}) manganates, because the XANES features are affected non-additively by the amount and distribution of the Jahn-Teller Mn^{3+} cations. The merit of the Combo method for the determination of manganese valence sums relative to the methods based on calibration curves is discussed.

Keywords: XANES, valence determination, phyllomanganates, tectomanganates, manganese oxides

Introduction

Manganates of nominal stoichiometry MnO_2 exist in many polymorphic forms and over a wide compositional range (Fig. 1). Layered manganates are commonly referred to as phyllomanganates or as birnessite-type compounds and those with a tunnel framework structure as tectomanganates. Apart from the two stoichiometric forms pyrolusite (β-MnO_2) and ramsdellite, which have tunnel dimensions of 1×1 and 2×1, respectively, all manganates have a charge deficit arising from low-valent manganese substitutions or from octahedral Mn vacancies that is balanced by various types of cations, such as alkali and alkaline earth metal ions (e.g., Li, K, Rb, Cs, Ca, Ba, Ra) and hydrolyzable cations (e.g., Ni, Zn, Pb). The redox and sorption properties of manganates give them a decisive role in several biological systems, environmental processes, and technological applications. For example, phyllomanganates can be intercalated with various organic and inorganic compounds to form multilayer nanocomposites or pillared structures. They are widely used also as templates for the formation of octahedral molecular sieves with variable tunnel sizes that have demonstrated excellent properties in heterogeneous catalysis, hazardous waste remediation, and rechargeable battery technology (Thackeray 1997; Toupin et al. 2004; Wang et al. 2004, 2005, 2011; Cormie et al. 2010; Laatikainen et al. 2010; Lafferty et al. 2010; Nakayama et al. 2010; Tang et al. 2010; Yan et al. 2010, 2011; Kim et al. 2001; Pinaud et al. 2011).

Natural and synthetic manganates often involve mixtures of up to three valences (Mn^{2+}, Mn^{3+}, Mn^{4+}), which may coexist in a single mixed-valent phase or be distributed between several species in a mixture. In both cases, it is therefore important to be able to determine the proportions of each valence state in situ, as opposed to measuring the average valence, for example by wet chemistry (Lingane and Karplus 1946; Vetter and Jaeger 1966). This information can be obtained from the analysis of the manganese $L_{2,3}$ and oxygen *K*-edges using electron energy loss near-edge (ELNES) or X-ray absorption near-edge structure (XANES) spectroscopy (Kurata and Colliex 1993; Mansot et al. 1994; Garvie and Craven 1994b; Bridges et al. 2000, 2001; McKeown and Post 2001; McKeown et al. 2003; Gilbert et al. 2003; Pecher et al. 2003; Glatzel et al. 2004; Riedl et al. 2006; Loomer et al. 2007; Ito et al. 2011). Several ELNES methods have been proposed. Among them, the two that seem to work best are: (1) the difference between Mn L_3 and oxygen *K* energies, i.e., ΔE(Mn L_3-O *K*) vs. valence; and (2) a linear combination fit (LCF) to a set of pure-valence references (Zhang et al. 2010). The accuracy for the quantification of average Mn valence in

* E-mail: Alain.Manceau@obs.ujf-grenoble.fr
† Present address: BRGM, 3, avenue Claude Guillemin, 45060 Orléans Cedex 2, France.

0003-004X/12/0506–816$05.00/DOI: http://dx.doi.org/10.2138/am.2012.3903

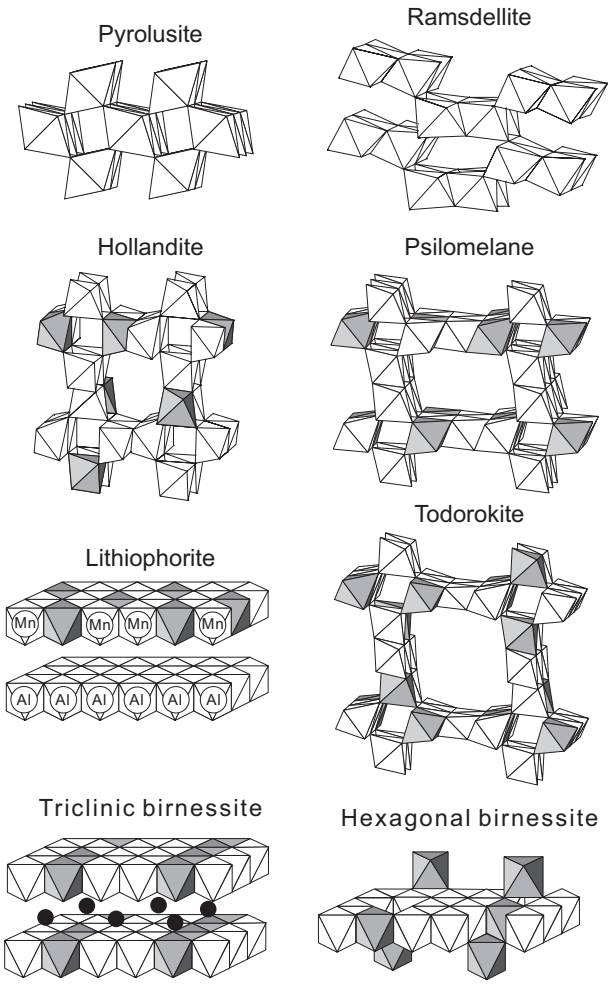

FIGURE 1. Polyhedral representation of the main types of tectomanganates (pyrolusite, ramsdellite, hollandite, psilomelane = romanechtite, todorokite) and phyllomanganates (birnessite, lithiophorite). Octahedra occupied by Mn^{3+} cations are in gray.

the range of 3+ to 4+, estimated from a set of synthetic cryptomelane (2 × 2 tectomanganate) standards, can be as good as ±0.02 valence units (v.u.) with the first method and ±0.03 with the second. However, as powerful as these methods are, none of them separately or together is totally satisfying. The error of the ΔE(Mn L_3-O K) calibration curve is larger in the presence of other heterovalent cations such as Fe^{3+}, a common impurity in natural materials, because the position of the oxygen K-edge is affected by all oxygen bonding environments in the structure, including those in any waters of hydration. Results depend also to some extent on the selection of the assumed end-members (e.g., pyrolusite vs. ramsdellite), presumably because various arrangements of Mn octahedra give rise to different shapes of ELNES spectra (Zhang et al. 2010), as reported for XANES (Manceau et al. 1992). The slightly lower accuracy of the LCF method relative to ΔE(Mn L_3-O K) (±0.03 vs. ±0.02) is, however, somehow compensated by its ability to estimate the fraction of Mn^{2+}, in addition to Mn^{3+} and Mn^{4+} from the weight of each fit component, provided the appropriate reference spectra are chosen.

The valence states of Mn in mixed-valent manganates can be obtained also by K-edge XANES spectroscopy (Manceau et al. 1992; Ammundsen et al. 1998; Ressler et al. 2000; Jokic et al. 2001; Villalobos et al. 2003; Ramallo-Lopez et al. 2004; Gunter et al. 2002, 2004, 2006; Bargar et al. 2005; Farges 2005; Figueroa et al. 2005; Negra et al. 2005; Webb et al. 2005; Saratovsky et al. 2006; Chaboy 2009; Chalmin et al. 2009; Grangeon et al. 2010; Rumble et al. 2010). Considering the large variability in structural and chemical compositions of manganates, not easily accessible to measurement, one might then ask whether there are features of the XANES that are independent enough of the exact species to be useful in quantitating mixtures and heterovalent manganates. This first question was addressed by recording high-quality XANES spectra from a large series of well-characterized Mn compounds (Table 1), which include many of the distinct stoichiometries and polyhedral arrangements described in the literature, and by defining "valence state fingerprints" from the spectral derivatives that are ideally unique to specific Mn oxidation and almost independent of the manganate structure.

The identification of valence state fingerprints leads to the second question of whether they are distinct enough to determine, with good precision, the fractions of each valence in a mixed-valent system. To answer this question, the XANES spectra of aliovalent manganates with known structure and chemical formula were fit to linear combinations of pure Mn species. We show that the unknown amounts of Mn 2+, 3+, and 4+ can be obtained when: (1) the whole set of pure-valence references is included in the LCF, regardless of their chemical and polyhedral similarity with the unknown; (2) all unphysical negative loadings of the references are rejected from the regression; and (3) the n+ fraction in the unknown is taken as the sum of all positive fractions obtained for the n+ references (n = 2,3,4). The accuracy of the proposed method for tectomanganates and phyllomanganates containing no or little Mn^{3+} in the layer and less than ~15% Mn^{2+} is 0.04 v.u., as determined by applying this method to well-characterized mixed-valent materials, therefore close to that obtained with ELNES. However, this method presents the

TABLE 1. List of pure-valence references

Standard	Code name	Formula	Mn valence	Source/ Reference
Pyrolusite	REF4-1	β-MnO_2	4.0	Nassau, Germany
Ramsdellite	REF4-2	MnO_2	4.0	
$Ca_2Mn_3O_8$	REF4-3	2/3 $Ca_2Mn_3O_8$ + 1/3 $CaMnO_3$	4.0	
KBi	REF4-4	$K^+_{0.296}(Mn^{4+}_{0.926}\square_{0.074})O_2{\cdot}0.40H_2O$	4.0	Gaillot et al. (2005)
Groutite	REF3-1	α-MnOOH	3.0	Minnesota, U.S.A.
Feitknechtite	REF3-2	β-MnOOH	3.0	Manceau et al. (1992)
Manganite	REF3-3	γ-MnOOH	3.0	
Mn_2O_3	REF3-4	Mn_2O_3	3.0	
$MnPO_4$	REF3-5	$MnPO_4$	3.0	
Hureaulite	REF2-1	$Mn_5(PO_4)[PO_3(OH)]_2{\cdot}4H_2O$	2.0	
Fungi	REF2-2	Mn^{2+}-sorbed fungi	2.0	Grangeon et al. (2010)
Rhodocrosite	REF2-3	$MnCO_3$	2.0	
Manganosite	REF2-4	MnO	2.0	
Pyroxmangite	REF2-5	$(Mn,Fe)SiO_3$	2.0	Manceau and Gallup (2005)
Tephroite	REF2-6	Mn_2SiO_4	2.0	Manceau and Gallup (2005)
$MnSO_4$aq	REF2-7	Solvated Mn^{2+}, aqueous solution	2.0	
$MnSO_4$s	REF2-8	$MnSO_4{\cdot}xH_2O$	2.0	Alfa Aesar-010807

Note: □ = vacancy.

advantage of not requiring educated choices on the relevance of a particular reference used in the LCF. Finally, by making the database openly available as Supplementary material[1], we aim to provide a useful resource for others.

Experimental methods

Measurements

All spectra are from beamline 10.3.2 at the Advanced Light Source and were acquired with procedures similar to those described in Marcus et al. (2008). The energy was referenced to the first inflection point in metallic Mn at 6537.7 eV (Kraft et al. 1996). With this calibration, the second peak in the derivative of the signal occurs at 6540.9 eV for Mn^{3+} and Mn^{4+} compounds. The uncertainty in energy is 0.1 eV. To facilitate normalization and possibly make use of EXAFS-region information, data were taken out to 300 eV above the edge.

To reduce overabsorption, many of the references were run in total electron yield mode. For others, fluorescence yield was used on small particles and the consistency of results checked from particle to particle. In some cases, there were inter-particle variations that could not be ascribed to varying amounts of overabsorption; they were attributed to dichroism in single-crystal grains, so we used the average over several particles in the database. Radiation damage was checked for by comparing successive scans on a spot. For some samples, QuickXANES was used to acquire data with minimal beam damage per spot. For the aqueous $MnSO_4$ solution (1 wt% in DI water), the microprobe beam caused the accumulation of Mn at the irradiated spot; closing down slits in front of the focusing mirrors allowed us to attenuate the beam enough to let us use QuickXANES to get consistent spectra without this radiation-induced accumulation.

Data handling

The data were deadtime-corrected, energy calibrated, pre-edge subtracted and post-edge normalized, and analyzed using the software available from the beamline web site. The pre-edge subtraction and post-edge normalization procedures are shown in Supplementary Figure 1[1]. The reliability of the linear-combination method was verified by fitting the data from mixed-valent compounds in the ranges between 6521–6653 and 6535–6570 eV.

Results and discussion

Valence states fingerprint

Among the 17 reference spectra, the energy at which the absorption rises to half its post-edge value increases by 3.3 ± 0.9 eV from Mn^{2+} to Mn^{3+} and by 3.0 ± 0.6 eV from Mn^{3+} to Mn^{4+} (Fig. 2a). With a precision on the energy measurement of ±0.1 eV, this chemical shift allows differentiation of the three oxidation states in single-valent samples. Quantitative analysis of multicomponent spectra from polyvalent samples is, however, clearly hindered by the large variability among spectra from the same valence group, especially for the 2+ group. It is preferable to work with the first derivative of the absorbance ($d\mu/dE$) because it generally shows the spectroscopic structure more clearly than the absorption spectrum, and small errors in the post-edge normalization do not change the shape of the derivative (Fig. 2b).

The (Mn^{3+}, Mn^{4+}) manganate spectra from the database show that trivalent Mn is reflected phenomenologically on the first derivative in a decrease of the amplitude at 6555.0–6560.0 eV from the Mn^{4+} component, and an increase at 6547.9–6549.0 eV from the Mn^{3+} component (Fig. 3a). For example, the spectrum for todorokite_SAF, with a nominal mean valence of 3.73 (Table 2) (Post et al. 2003), is intermediate between those of the Mn^{4+} phyllomanganate reference KBi and the Mn^{3+} references groutite (α-MnOOH) and feitknechtite (β-MnOOH; Fig. 3b). Comparison of the spectra for 2 × 2 (hollandite), 2 × 3 (psilomelane), and 3 × 3 (todorokite) tectomanganates shows that the ratio of the amplitudes at the two "indicator" regions is sensitive to a variation of a few hundredths valence units (v.u.) (Fig. 4a; Table 2). The best two-component fit of the todorokite_SAF derivative was obtained with 0.58 KBi + 0.37 β-MnOOH, corresponding to the unrealistically low average valence of 3.58–3.61 (Fig. 5a). This low value and the relatively poor quality of the fit, with a normalized sum-squared residual (*NSS*) of 3.7 10^{-2}, show that the Mn *K*-edge spectra of tectomanganates cannot be modeled as weighted sums of only two end-member spectra.

Divalent Mn in (Mn^{2+}, Mn^{3+}, Mn^{4+}) manganates is indicated on the XANES derivative by a leftward shift of the rising slope at 6542–6547 eV relative to tectomanganates and (Mn^{3+}, Mn^{4+})

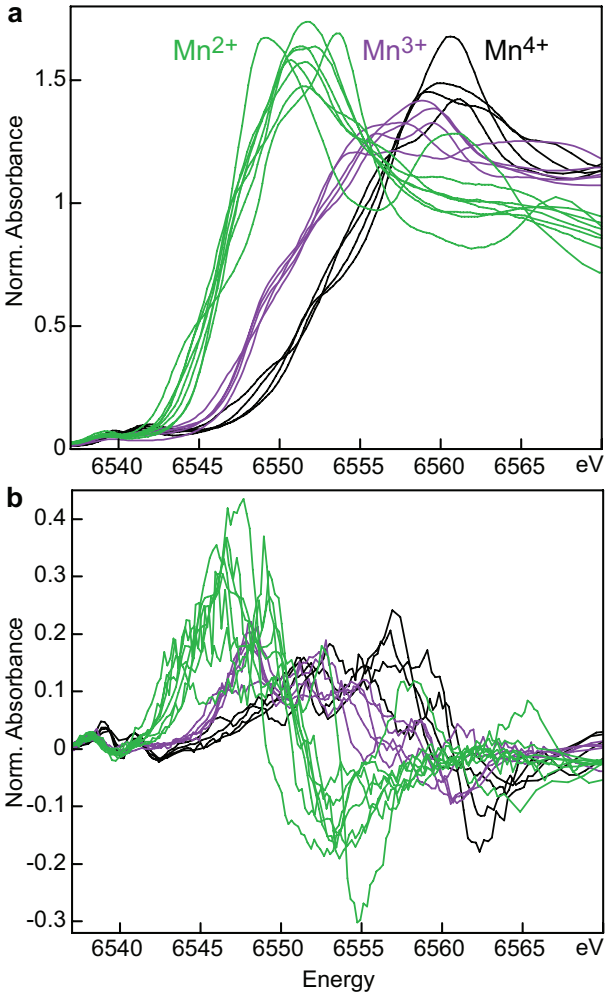

Figure 2. XANES absorption spectra (**a**) and first derivatives (**b**) of single-valent Mn^{2+}, Mn^{3+}, and Mn^{4+} species in the database. For clarity, spectra are not identified individually, but can be freely downloaded from the supplementary materials[1].

[1] Deposit item AM-12-037, Supplementary data, tables, and figures in PDF and two ASCII files (Mn XANES database). Deposit items are available two ways: For a paper copy contact the Business Office of the Mineralogical Society of America (see inside front cover of recent issue) for price information. For an electronic copy visit the MSA web site at http://www.minsocam.org, go to the American Mineralogist Contents, find the table of contents for the specific volume/issue wanted, and then click on the deposit link there.

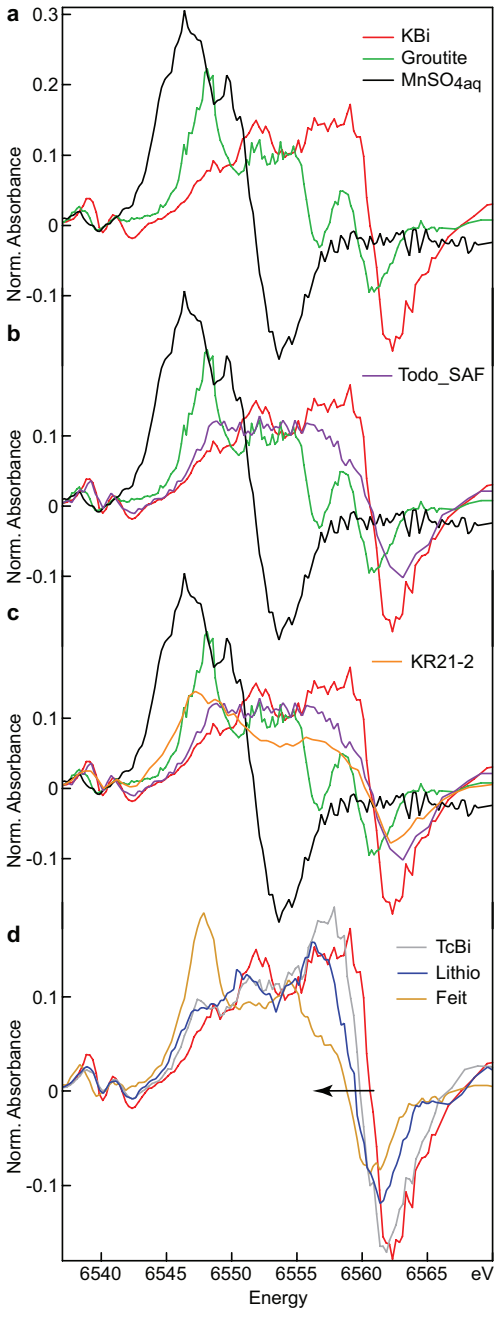

FIGURE 3. First derivative XANES absorption spectra of a selection of single- and mixed-valent Mn species.

phyllomanganates (Figs. 3c, 4b, and 4c). Using hexagonal birnessite HBi5 as a three valence state reference, the visual detection limit of Mn^{2+} is about 5% of the total Mn (Table 2). This diagnostic spectral feature is not captured when the HBi5 spectrum is reconstructed with a linear combination of pure-valence (phyllo-, tecto-) manganate species. The best model-fit with three components from the entire database yields 0.21 ramsdellite (Mn^{4+}) + 0.38 KBi (Mn^{4+}) + 0.37 β-MnOOH (*NSS* = 1.8 10^{-2}), that is 59–61% Mn^{4+} and 37–39% Mn^{3+}, in disagreement with the nominal composition of $Mn^{4+}_{0.722}Mn^{3+}_{0.22}Mn^{2+}_{0.055}$ (Fig. 5b) (Lanson et al. 2000).

So far, all examined mixed-valent manganates exhibited intermediate spectral features that could be explained empirically by direct comparison with end-members. This is not the case when Mn^{3+}, a Jahn-Teller cation, is incorporated in the manganese layer, as in triclinic birnessite (TcBi) and lithiophorite, and not dominantly in the interlayer, as in HBi. TcBi and lithiophorite have a maximum at 6556.3–6558.0 eV, which is absent from KBi8 and β-MnOOH, the two closest phyllomanganate end-members (Fig. 3d). In addition, TcBi and lithiophorite have distinct derivatives, although similar amounts of layer Mn^{3+}: 31% and 33%, respectively. The layer strain induced by the Jahn-Teller effect is reduced in TcBi by the ordering in rows of the Mn^{3+} ions among the lattice of Mn^{4+}, the stripe layer having an orthogonal symmetry (Drits et al. 1997; Lanson et al. 2002). In contrast, the layer distortion is reduced in lithiophorite by the avoidance of Mn^{3+}-O-Mn^{3+} links resulting in an even distribution of the two types of cations and a hexagonal symmetry of the layer (Manceau et al. 2005). These defects, and their minimization, affect the structure, and thus the XANES, in a non-additive way relative to the Mn^{4+}-pure and Mn^{3+}-pure end-members. Synergistic effects of various defects on the structure and XANES also occur in manganites (Chaboy 2009). Although the XANES spectra of (layer Mn^{3+}, Mn^{4+}) phyllomanganates cannot be modeled, even semi-quantitatively, as a weighted sum of single-valence end-members, they have distinctive spectral features that can be used to speciate Mn in unknown materials. One of those is a leftward shift of $d\mu/dE = 0$ in the 6559.0–6560.5 eV interval with increasing Mn^{3+} in the layer (Fig. 3d).

In summary, Mn *K*-edge XANES is sensitive to the oxidation state and bonding environment of Mn in polyvalent manganates, and spectral fingerprints were defined that can be used to speciate the manganese forms in an unknown compound. However, the assumption that the XANES of mixed-valent manganates can be modeled simply by weighting the spectra of the structurally and chemically closest end-members does not hold. Is quantification nonetheless possible? Principal component analysis (PCA) with target transformation (TG) (Weiner et al. 1970; Hopke 1989; Malinowski 1991; Wasserman et al. 1999; Ressler et al. 2000; Manceau et al. 2002) are applied next, to determine which combination of pure-valence species may provide the correct valence composition in a mixed-valent manganate, if any.

Principal component analysis

The analysis was applied on the 12 mixed-valent tectomanganates and phyllomanganates with no or little layer Mn^{3+}, because their XANES are least affected by the short- and medium-range ordering of Mn (Table 2). The output parameters, including eigenvalues, the variance, the Malinowski (1977) indicator values (IND), and the variation of the fit total (normalized total sum-squared residual, *NSS-Tot*), are given in Supplementary Table 1[1] for the six most significant principal components (PCs).

The decline of the eigenvalues, which ranks PCs according to their importance in reproducing a data set, and IND, which usually reaches a minimum for the least significant component, both identified three PCs (Supplementary Fig. 2 and Table 1[1]). The first component represents features common to all spectra

TABLE 2. List of mixed-valent compounds

Compound	Formula	Average Mn valence		Source/Reference
		Formula	Titration*	
		Tectomanganate		
Hollandite			3.75–3.83†	Frondel et al. (1960)
Psilomelane‡			3.75–3.75†	Hufgard, Germany
Todorokite_Japan			3.72–3.73†	
Todorokite_SAF	$Mg_{0.45}Na_{0.42}Ca_{0.15}K_{0.01}(Mn^{4+}_{4.38}Mn^{3+}_{1.62})O_{12}\cdot 4H_2O$	3.73		South Africa, Post et al. (2003)
		Phyllomanganate with no/little layer Mn^{3+}		
KBi8	$K_{0.231}Mn^{3+}_{0.077}(Mn^{4+}_{0.885}\square_{0.115})O_2\cdot 0.6H_2O$	3.92	3.87	Gaillot et al. (2003)
HBi5	$Mn^{3+}_{0.11}Mn^{2+}_{0.055}H^{+}_{0.33}(Mn^{4+}_{0.722}Mn^{3+}_{0.11}\square_{0.167})O_2\cdot 0.5H_2O$	3.66		Silvester et al. (1997); Lanson et al. (2000)
KR21-2	$Mg_{0.04}K_{0.03}Mn^{3+}_{0.25}(Mn^{4+}_{0.78}\square_{0.22})O_2\cdot nH_2O$§ $Mn^{2+}_{0.15(5)}Mn^{3+}_{0.10(10)}Mn^{4+}_{0.73(10)}$‖			Fungal phyllomanganate, Grangeon et al. (2010)
KR21-Cu-A, B				Fungal phyllomanganate treated with 10 *mM* $CuSO_4$ (A) and rad-damaged (B).
SP6-Cu-A, B, C				Bacterial phyllomanganate treated with 10 *mM* $CuSO_4$ (A) and rad-damaged (B, C).
		Phyllomanganate with layer Mn^{3+}		
KBi10	$K_{0.314}(Mn^{4+}_{0.737}Mn^{3+}_{0.246}\square_{0.017})O_2\cdot 0.5H_2O$	3.75	3.67	Gaillot et al. (2007)
TcBi	$Na_{0.31}(Mn^{4+}_{0.69}Mn^{3+}_{0.31})O_2\cdot 0.4H_2O$	3.69		Lanson et al. (2002)
Lithiophorite	$(Al_{0.67}Li_{0.32})(Mn^{4+}_{0.68}Mn^{3+}_{0.32})O_2(OH)_2$	3.68	3.67–3.67†	Manceau et al. (2005)
		Other		
Hausmannite	Mn_3O_4	2.67		

* Potentiometric titration using $(NH_4)_2Fe(SO_4)$ Mohr salt and sodium pyrophosphate (Lingane and Karplus 1946; Vetter and Jaeger 1966). □ = vacancy.
† Duplicate.
‡ Fraction of Mn^{2+} = 0.05. Also named romanechite.
§ From X-ray diffraction. This technique is not sensitive to residual Mn^{2+} not oxidized by fungi.
‖ Bulk fractions of Mn 2+, 3+ and 4+ from XANES, with estimated uncertainty in parenthesis.

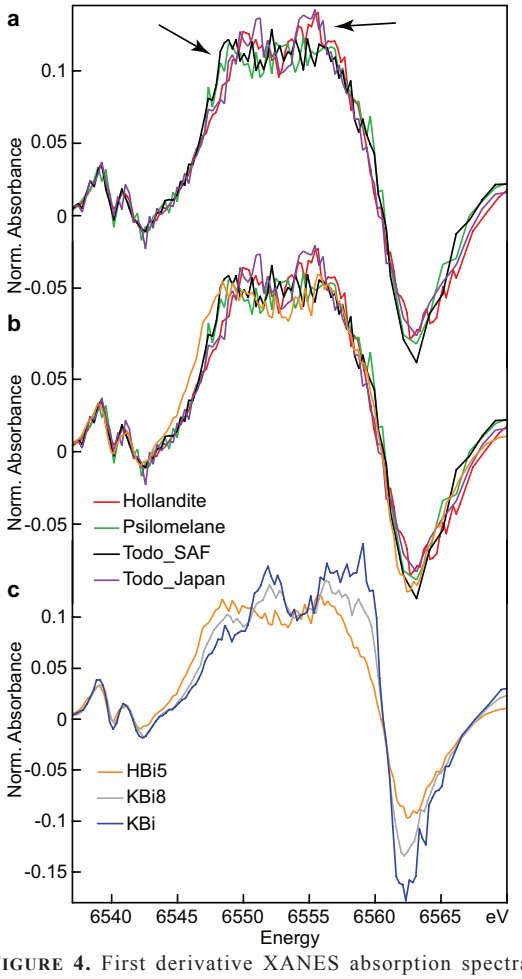

FIGURE 4. First derivative XANES absorption spectra of phyllomanganates and tectomanganates with various proportions of Mn^{2+} and Mn^{3+}.

and has approximately the same loading for all spectra. This component accounts for 85.8% of the "strength" of the derivative signal. The other 14.2% is the contribution from differences (i.e., variance) between spectra including noise. The next two components account for 13.1 + 0.8 = 13.9%. That is, the sum-squared (norm) of the part of the reconstructed signal that comes from the second and third component is 13.9% of the whole, which is 13.9/14.2 = 98% of the variance between XANES derivative spectra.

Deviations between data and reconstructions based on three PCs were small with normalized sum-squared (*NSS*) values from 2.4 to 8.3 10^{-3}, and a *NSS-Tot* of 5.4 10^{-3}. Therefore, the series of manganates can be described well with variable proportions of only three model compounds, which theoretically can be identified from a database by target transformation, provided the unknown is present in the library of reference spectra. Target testing of a reference goes beyond the fingerprinting approach between known and unknown spectra, because the entire data set is analyzed at one time in a statistically meaningful way for similarity to a specific structural reference. This similarity was evaluated with the normalized sum-squared residual (*NSS*) between the tested reference and its target transform, and with the *SPOIL* value (Malinowski 1978). Usually, references with *SPOIL* values <1.5 are considered excellent, 1.5 to 3 good, 3 to 4.5 fair, 4.5 to 6 poor, and >6 unacceptable.

Out of the 17 pure species contained in the database, one Mn^{4+} reference fell into the *SPOIL* category excellent (KBi), and three were fair to poor (Supplementary Table 2 and Fig. S3[1]). Neither groutite (α-MnOOH, 2 × 1 tunnel structure) nor manganite (γ-MnOOH, 1 × 1) passed the test successfully, although they were supposedly a good structural proxy for tectomanganates and for phyllomanganates with interlayer Mn^{3+} octahedra bonded by shared corners to the manganese layer. This result explains why the valence composition of todorokite_SAF and HBi5 could not be obtained previously from a two- or three-

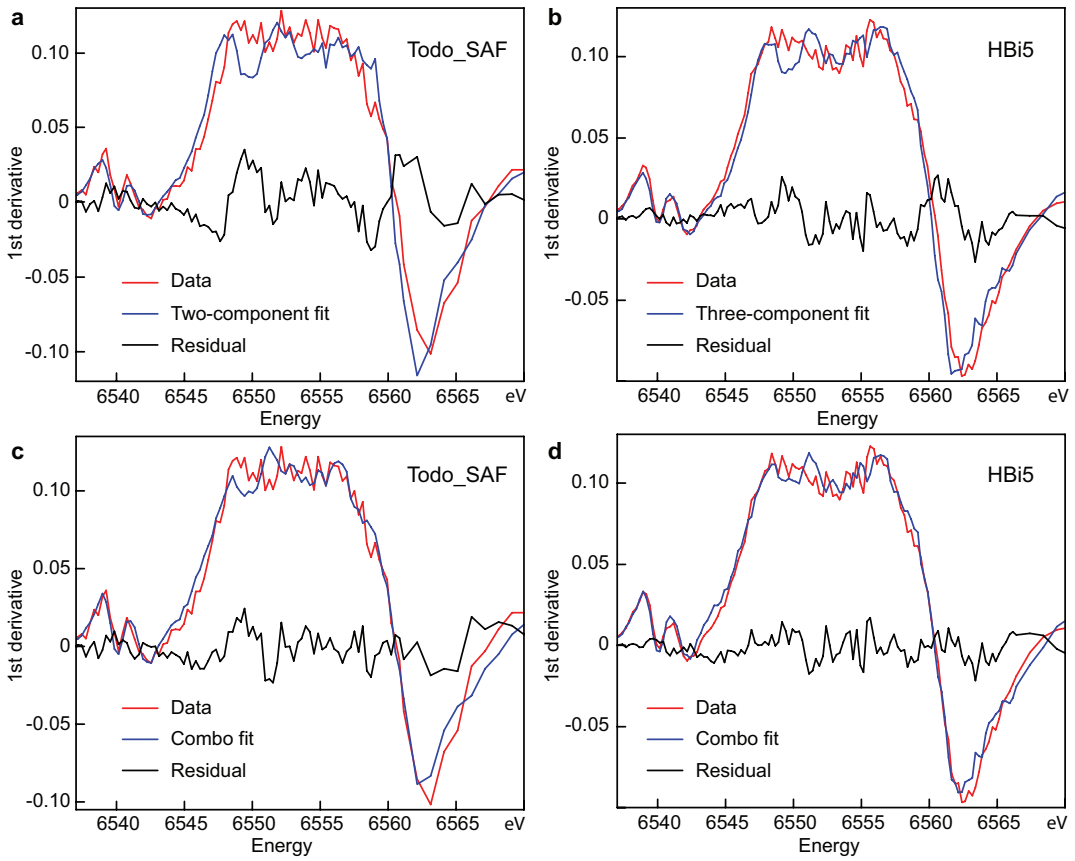

Figure 5. (**a**) Best two-component fit of todorokite_SAF. (**b**) Best three-component fit of HBi5. (**c** and **d**) Same spectra fitted with the Combo method.

component unconstrained fit of all the pure-valence references in the database. More generally, the above exercise shows that there are not really idealized Mn^{2+}, Mn^{3+}, and Mn^{4+} spectra that can be mixed in various proportions to model the spectra of real mixed-valent materials. As will be shown below, the valence fractions and average oxidation state can be obtained when all pure-valence species are included in the fit, so as to include in the regression all distinct bonding environments contained in the database and plausibly present in the unknown.

Linear combinations with a database of pure-valence species (the Combo method)

Some methods for analyzing valence states, such as fitting the pre-edge peaks, rely on a few features of a small region of the spectrum (Farges 2001; Galoisy et al. 2001; Petit et al. 2001; Wilke et al. 2001; Berry et al. 2003). Such methods tend to do well in classifying single species by valence, or extracting the average valence, but are less able to extract the fractions of multiple valence states, as the case with manganese (Farges 2005; Chalmin et al. 2009). Part of the reason for this is that the spectra of different species with a given valence can look quite different. To solve the difficult problem of quantifying multiple valence states, it seems necessary to use as much information as possible, thus the whole spectrum out to some reasonable distance from the main edge. Also, because there is a significant variability between species with the same valence, any purely empirical method must be developed with reference to as large a set of known references as possible.

Consider the following proposed method: Fit the unknown spectrum to a linear combination of all the reference spectra, and evaluate the fraction of Mn in, say, the Mn^{2+} state as the sum of fractions of each species in the fit times the fraction of divalent Mn in each species. It is tautologically obvious that if the unknown is actually one of the references, the correct answer will be obtained. Furthermore, a spectrum corresponding to a mixture of known references will "read" as a valence mixture appropriate to the input mix. Thus, this method works perfectly to "interpolate" between known references. If this method is applied to a true unknown, it will often yield unphysical negative loadings (fractions of species) for many of the references. If, for instance, two of the references are similar to each other, one can get loadings of opposite sign and large and almost equal magnitude, as the fit "tries" to work with the small difference between the two references. Furthermore, the fits become very noisy because the fitting problem is ill-conditioned. To avoid these problems, we have to constrain the loadings to be non-negative.

We applied this non-negativity constraint in two different ways and obtained the same results. In one method, we did an unconstrained linear fit to a sum of all the references, and then progressively eliminated references with negative loadings in

ascending order of loading. Note that when one component is eliminated, the loadings of all others change. After all negative loadings were eliminated, each reference previously deleted was reselected randomly one-by-one to ensure that the global minimum was found rather than a local minimum using *NSS* as best-fit criterion (Supplementary Fig. S4[1]). In the other method, we tested all combinations of six or fewer references with positive loadings and chose the one that gave the best fit. The choice of six for the maximum number of components was governed simply by practical limits of the algorithm used. Because both procedures yielded identical or near-identical results, we refer to both as the Combo method. Changing the fit interval had little effect on the results from the derivatives [Δ(val) = 0.01 v.u.; Supplementary Tables 2 and 3[1]], but changed the results from the XANES absorption spectra by as much as 0.03 v.u. due to some inevitable arbitrariness in the slope of the post-edge line during data normalization. This affect was compensated by including a post-edge slope as a free parameter for XANES data fitted in the 6521–6653 eV interval. A measure of the internal consistency of the method can be obtained by comparing the results from the XANES spectra and their derivatives. The differences between average valences derived using the two forms of the spectra is 0.01 v.u. for (Mn^{3+}, Mn^{4+}) manganates, and 0.03–0.08 v.u. when the fraction of Mn^{2+} is higher than ~0.15 (Table 3 and Supplementary Table 4[1]).

The spectral fingerprints defined previously on derivatives are reproduced in the fits (Figs. 5c and 5d), and the average valences and fractions now coincide to at least 0.08 and often within 0.03–0.04 with chemical and structural values where available (Table 3 and Supplementary Table 5[1]). The greatest differences between XANES-estimated and predicted Mn valences are observed with the birnessites HBi5 (0.05 v.u.) and KBi8 (0.08 v.u.), and may be real because birnessites are metastable (Gaillot et al. 2004) and their structural formulas were established 9 to 12 years ago (Lanson et al. 2000; Gaillot et al. 2003). Indeed, the ratio of interlayer Mn^{3+} to layer Mn^{4+} of phyllomanganates increases with aging (Grangeon 2009) and they tend to transform into tectomanganates with time (Cui et al. 2010). We conclude that the accuracy for determination of average Mn valence for the range of 3+ and 4+ by the Combo method is 0.04 v.u.

One may ask what the error bars are on the fractions of each reference species (Supplementary Tables 2 and 3[1]), and attempt to derive them using the usual statistical methods. However, there is a conceptual problem with this approach to error estimation. Unlike in the usual sort of linear combination fitting, we do not assert that the unknowns are actually mixtures of the reference materials or even of materials that are structurally like the references, nor do we assert that the fits we get are always good representations of the data. In fact, some of the fits (e.g., for hausmannite, vide infra) are quite poor. Therefore, it makes no sense to assign error bars to the loadings of individual components. Rather, what we contend is that the empirical method described here yields the correct average valences to within about 0.04 v.u. in tectomanganates and phyllomanganates containing no or little Mn^{3+} in the layer and less than ~15% Mn^{2+}, and the correct fractions of the valence states to within 4.4% (σ = 2.6%) in the 6535–6670 eV interval (Table 3) and 4.6% (σ = 2.9%) in the 6521–6653 eV interval (Supplementary Table 4[1]), when applied to the collection of mixed-valent materials available to us.

Application of the Combo method to the photo-reduction of Mn^{4+} to Mn^{2+} in phyllomanganates

Poorly crystallized phyllomanganates, either biogenic or abiotic, are highly sensitive to electron (Garvie and Craven 1994a) and X-ray (Bargar et al. 2005) beam-induced damage (Manceau et al. 2002). In this process, Mn^{4+} is reduced to Mn^{2+}, but uncertainty remains if the reduction proceeds in one step (i.e., two-electron transfer) or two steps (i.e., two sequential

TABLE 3. Fractional and average valence states of Mn obtained from the Combo fit of XANES spectra and derivatives in the 6535–6570 eV interval

	Fractional Mn^{4+}		Fractional Mn^{3+}		Fractional Mn^{2+}		Average Mn valence	
	XANES	Structure	XANES	Structure	XANES	Structure	XANES	Structure/Titration
				XANES				
Hollandite	0.81	–	0.19	–	–	–	3.81	3.75–3.83
Psilomelane	0.76	–	0.24	–	–	–	3.76	3.75–3.75
Todorokite_Japan	0.77	–	0.23	–	–	–	3.77	3.72–3.73
Todorokite_SAF	0.70	0.73	0.30	0.27	–	–	3.70	3.73
KBi8	0.84	0.92	0.16	0.08	–	–	3.84	3.87–3.92
HBi5	0.66	0.72	0.29	0.22	0.05	0.05	3.61	3.66
KR21–2	0.58	–	0.28	–	0.14	–	3.45	–
KR21-Cu-A	0.76		0.16		0.08		3.67	
KR21-Cu-B	0.06		0.61		0.33		2.73	
SP6-Cu-A	0.71		0.13		0.16		3.56	
SP6-Cu-B	0.11		0.53		0.36		2.76	
SP6-Cu-C	0.03		0.39		0.59		2.44	
				First derivative				
Hollandite	0.82	–	0.16	–	0.02	–	3.81	3.75–3.83
Psilomelane	0.81	–	0.16	–	0.04	–	3.77	3.75–3.75
Todorokite_Japan	0.78	–	0.21	–	0.01	–	3.78	3.72–3.73
Todorokite_SAF	0.75	0.73	0.23	0.27	0.03	–	3.72	3.73
KBi8	0.84	0.92	0.14	0.08	0.01	–	3.83	3.87–3.92
HBi5	0.69	0.72	0.24	0.22	0.07	0.05	3.62	3.66
KR21-2	0.61	–	0.23	–	0.16	–	3.45	–
KR21-Cu-A	0.78		0.12		0.11		3.67	
KR21-Cu-B	0.16		0.49		0.35		2.81	
SP6-Cu-A	0.77		0.06		0.17		3.61	
SP6-Cu-B	0.20		0.42		0.38		2.83	
SP6-Cu-C	0.08		0.33		0.59		2.49	

one-electron transfers) via the transient formation of Mn^{3+}. If the second hypothesis is verified, then the question remains as to which of the two steps is rate limiting, the Mn^{4+} to Mn^{3+} or the Mn^{3+} to Mn^{2+} reduction? To address this question, two biogenic δ-MnO_2 samples, one produced by an *Acremonium*-like hyphomycete fungus (strain KR21-2) (Miyata et al. 2004) and another by *Leptothrix discophora* (strain SP-6) (Jürgensen et al. 2004), were exposed to the beam, initially at low X-ray fluence to minimize Mn reduction, then for several hours with a full beam to photo-reduce manganese.

The Mn *K*-edges of the two samples changed shape and the peak maximum shifted to lower energy values as irradiation proceeded (Figs. 6a and 6b). With increasing fluence, the peak position shifted from an Mn^{4+}-like maximum at 6560.7 eV to an Mn^{3+}-like maximum at 6558.2 eV, and its shape became asymmetrical with a shoulder at the Mn^{2+}-like maximum of about 6551.0 eV. At moderate reduction, Mn^{3+} increased from 12 to 49% (KR21-Cu-B) and 6 to 42% (SP6-Cu-B), and Mn^{2+} from 11 to 35% (KR21-Cu-B) and 17 to 38% (SP6-Cu-B) (Figs. 6c, 6d, and 7). Further irradiation (sample SP6-Cu-C) continued to increase the amounts of Mn^{2+}, but Mn^{3+} decreased from 42 to 33% at near completion of the Mn^{4+} reduction (8%). The predominance of Mn^{3+} at the beginning of the reaction, followed by the predominance of Mn^{2+} at the end of the reaction, both cations being minor species in the initial materials, means that only one electron is transferred at a time and the Mn^{3+} to Mn^{2+} step is rate limiting. Structurally, this limiting step likely corresponds to the migration of the reduced Mn^{3+} cations from within the phyllomanganate layer to the interlayer region (Silvester et al. 1997).

Application of the Combo method to other materials

The combination fit with a database procedure, or Combo method, presented here may be applied to other Mn materials, with the caveats that non-linearity effects may defeat the interpolation giving unrealistic values or poor data reconstruction. Figure 8 shows with the example of hausmannite (Mn_3O_4) that quite accurate valence fractions still can be obtained empirically if the loadings are constrained to be non-negative, even though the resulting fit is poor: $NSS = 5.2\ 10^{-3}$ compared to $10^{-5} \leq NSS \leq 10^{-4}$ for phyllomanganates and tectomanganates (Supplementary Table 2[1]). The Combo method yields 67% Mn^{3+} + 28% Mn^{2+} + 5% Mn^{4+} (average 2.76), in fair agreement with the formal valence composition of 2/3 Mn^{3+} and 1/3 Mn^{2+}, and in closer proximity to the actual value of 2.67 than the value of 2.86 derived from a linear fit with only MnO, Mn_2O_3, and MnO_2 (Fig. 8c). Thus, this method seems to capture some characteristics of the input

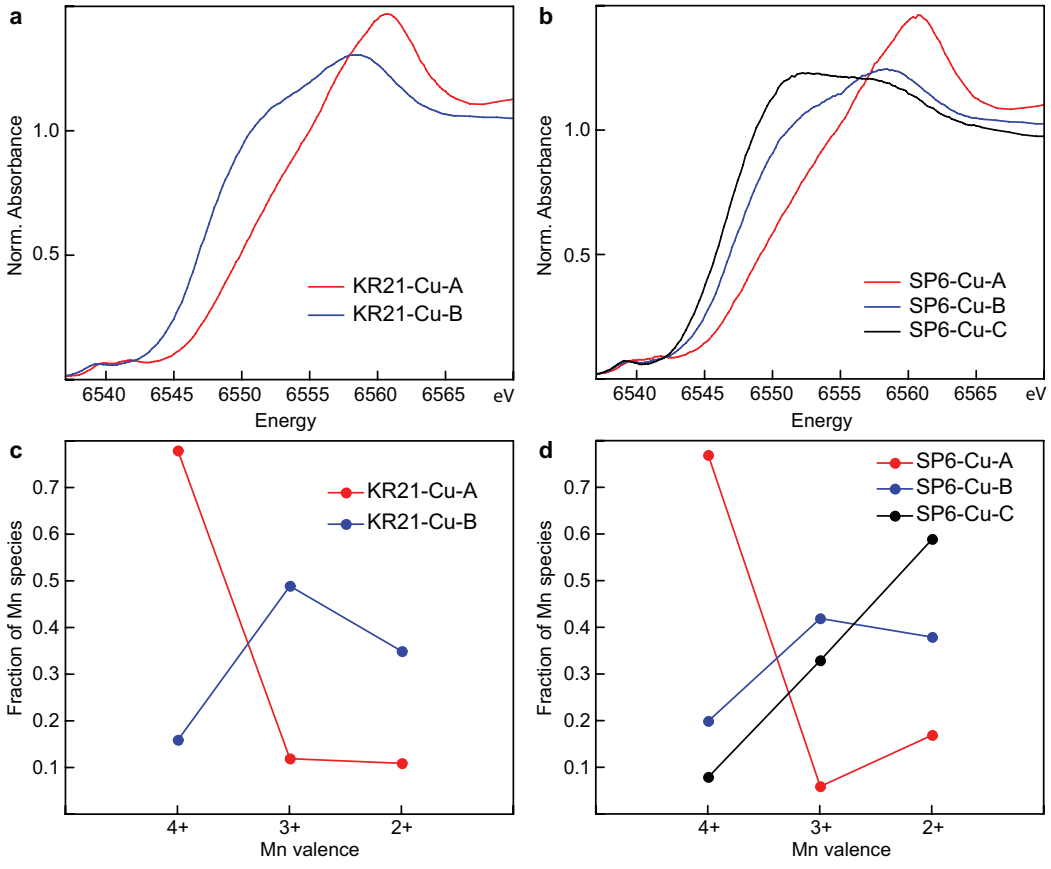

FIGURE 6. (**a** and **b**) XANES absorption spectra of two biogenic phyllomaganates at low (KR21-Cu-A, SP6-Cu-A), moderate (KR21-Cu-B, SP6-Cu-B), and high (SP6-Cu-C) X-ray fluence. (**c** and **d**) Evolution of the fractions of Mn^{4+}, Mn^{3+}, and Mn^{2+} at each accumulated X-ray fluence. The initial fraction of Mn^{2+} not oxidized by the enzymatic oxidation of Mn^{2+} to Mn^{4+} was removed by suspending the undamaged materials in 10 *mM* $CuSO_4$ overnight after synthesis, and washing it two times in deionized water (Adams and Ghiorse 1988).

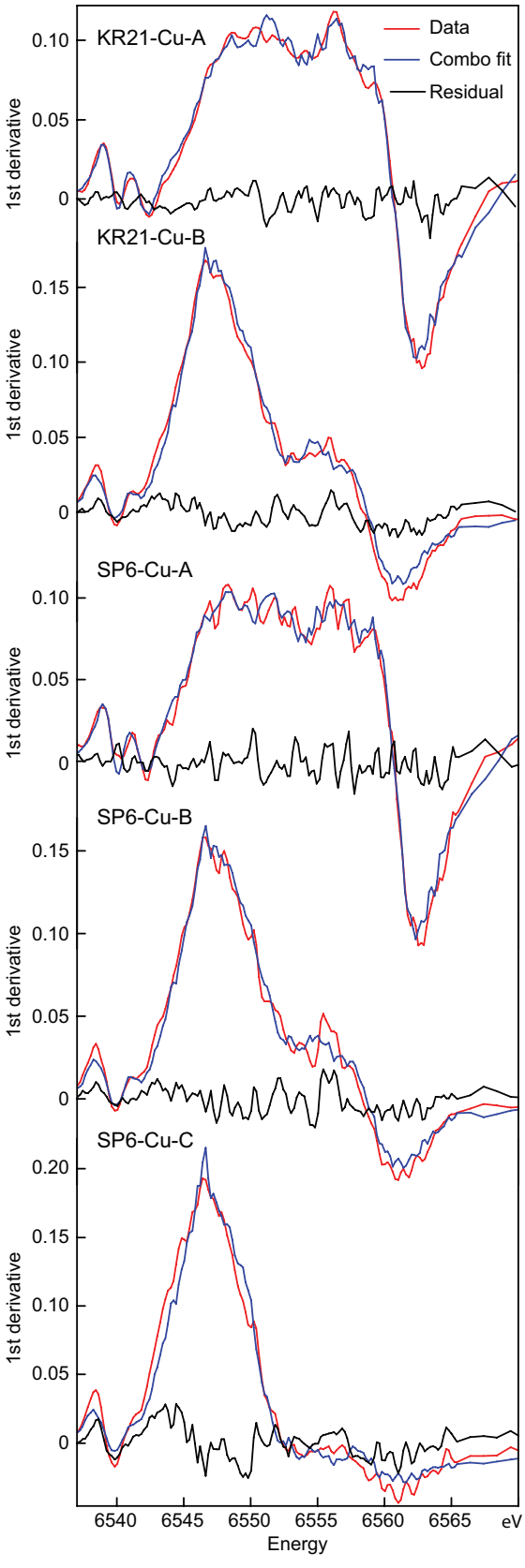

FIGURE 7. Combo fit of the biogenic XANES spectra.

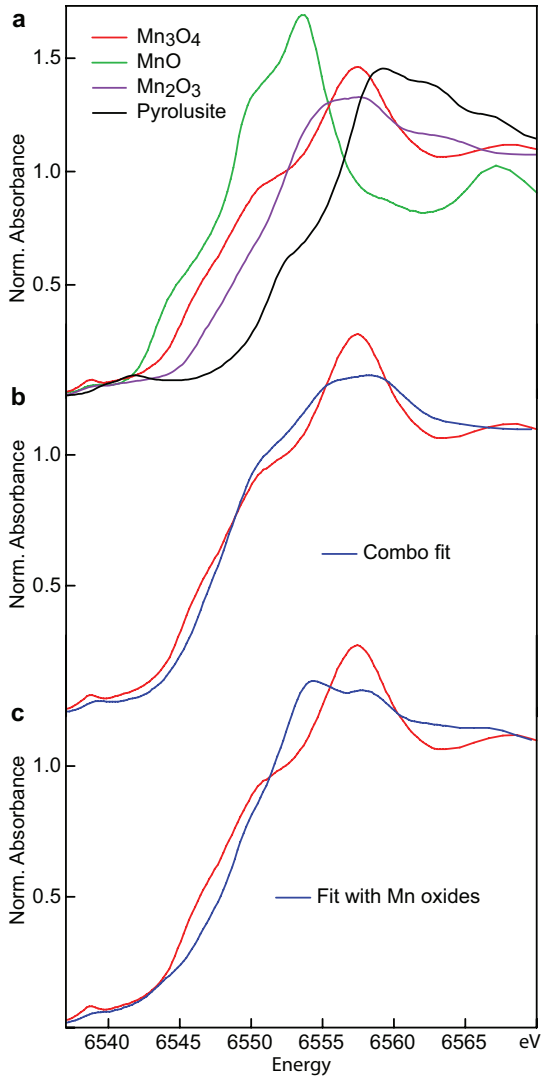

FIGURE 8. (**a**) XANES absorption spectra of Mn oxides. Best-fit of Mn_3O_4 with the Combo method (**b**) and with a linear combination of MnO, Mn_2O_3, and β-MnO_2 (pyrolusite) (**c**). Even when the fit is poor, the actual valence sum (2.67) is better extracted with the Combo method (2.76) than with a linear fit of the best chemically relevant references (2.86).

spectrum that correspond to the valence mixture, which otherwise are missed when the regression analysis is conducted with a limited set of model compounds that are chemically close but structurally distinct from the unknown materials.

Comparison with methods based on calibration curves

Continuing with Mn_3O_4, this mixed-valent oxide can be used to compare the precision of the average valence derived from the proposed method and from the usual calibration method, which correlates the valence to the energy position (or "chemical shift") of various features in the XANES spectra (Wong et al. 1984; Ressler et al. 1999, 2000; Ramallo-Lopez et al. 2004; Figueroa et al. 2005). An average valence of 2.43 is obtained when the absorption threshold is taken as the energy of the absorbance at $0.4 \leq \Delta\mu \leq 0.8$, and 2.30 from the energy position of the

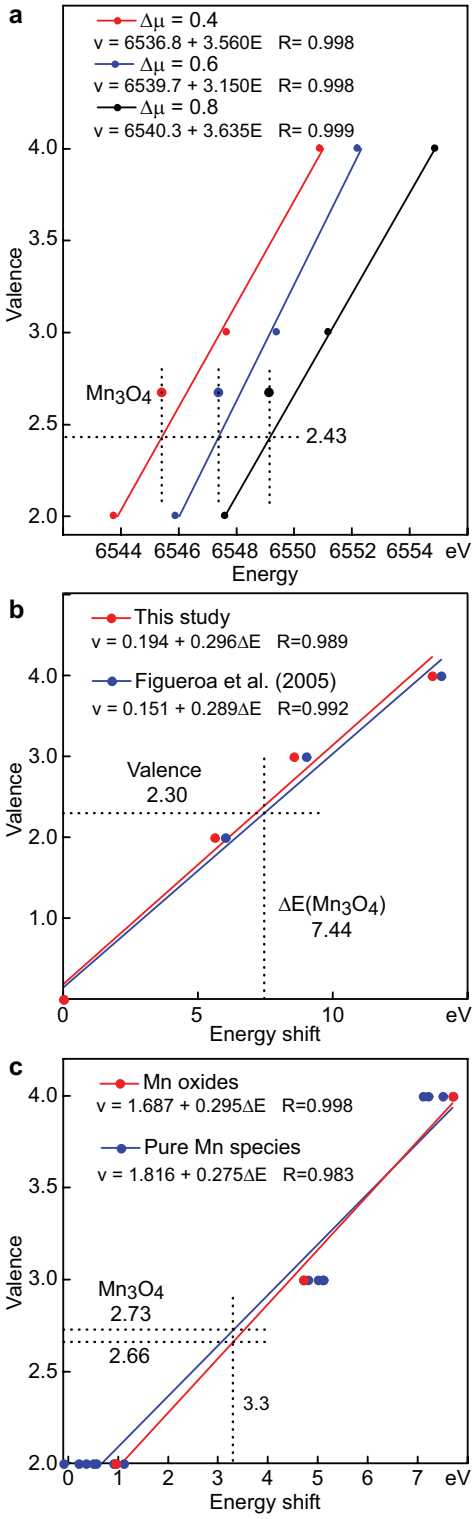

FIGURE 9. Determination of the average Mn valence of hausmannite (Mn_3O_4) using calibration curves calculated with MnO, Mn_2O_3, and MnO_2 (pyrolusite) as calibrants. The curves were calculated from the dependence on valence of the threshold energy at $\Delta\mu = 0.4$, 0.6, and 0.8 (**a**), the energy of the first peak in the first derivative (**b**), and the edge shift relative to the Mn foil calculated at 80% of the integrated absorption area [6550.95 eV; method of Capehart et al. (1995)] (**c**).

first peak in the derivative curve (Figs. 9a and 9b). These two valences are further apart from the nominal value of 2.67 than the value of 2.76 derived from the Combo method. Interestingly, the correct value (2.66 ± 0.01) is obtained using the calibration method of Capehart et al. (1995) and MnO, Mn_2O_3, and MnO_2 (pyrolusite) as calibrants (Fig. 9c; Supplementary Table 5[1]). When the calibration curve of Capehart is calculated with all the pure-valence references in the database, the average Mn_3O_4 valence is 2.73. Figure 9c shows that the loss in accuracy results from the large variability in the shape of the Mn^{2+} spectra, as seen from the dispersion of the y = 2 points on the x (energy) axis. The inclusion in the database of several references with the same oxidation state but a wide range of chemical structures facilitates the determination of the valence fractions by the Combo method, because the irrelevant references give negative loadings. In contrast, in the calibration method the effects of valence, site symmetry, coordination geometry, ligand electronegativity, and bond distances on various absorption features in the XANES spectra all contribute to the slope of the valence = f (energy) straight line. Therefore, the only way to improve tangibly the applicability of the calibration method is to gather independent estimates of the most likely local environments in the unknown material.

ACKNOWLEDGMENTS

Samples KR21-Cu and SP6-Cu were kindly provided by Naoyuki Miyata and Yukinori Tani. The ALS is supported by the Director, Office of Science, Office of Basic Energy Sciences, Materials Sciences Division of the U.S. Department of Energy under Contract No. DE-AC02-05CH11231 at the Lawrence Berkeley National Laboratory.

REFERENCES CITED

Adams, L.F. and Ghiorse, W.C. (1988) Oxidation state of Mn in the Mn oxide produced by *Leptothrix discophora* SS-1. Geochimica et Cosmochimica Acta, 52, 2073–2076.

Ammundsen, B., Jones, D.J., and Roziere, J. (1998) Effect of chemical extraction of lithium on the local structure of spinel lithium manganese oxides determined by X-ray absorption spectroscopy. Chemistry of Materials, 8, 2799–2808.

Bargar, J.R., Tebo, B.M., Bergmann, U., Webb, S.M., Glatzel, P., Chiu, V.Q., and Villalobos, M. (2005) Biotic and abiotic products of Mn(II) oxidation by spores of the marine *Bacillus sp.* strain SG-1. American Mineralogist, 90, 143–154.

Berry, A.J., O'Neill, H.St.C., Jayasuriya, K.D., Campbell, S.J., and Foran, G.J. (2003) XANES calibrations for the oxidation state of iron in a silicate glass. American Mineralogist, 88, 967–977.

Bridges, F., Booth, C.H., Kwei, G.H., Neumeier, J.J., and Sawatzky, G.A. (2000) Temperature dependent changes of the Mn 3d and 4p bands near Tc in colossal magnetoresistance systems: XANES study of $La_{1-x}Ca_xMnO_3$. Physical Review B, 61, R9237–R9240.

Bridges, F., Booth, C.H., Anderson, M.A., Kwei, G.H., Neumeier, J.J., Snyder, J., Mitchell, J., Gardner, J.S., and Brosha, E. (2001) Mn K-edge XANES studies of $La_{1-x}A_xMnO_3$ systems (A=Ca, Ba, Pb). Physical Review B, 63, 214405.

Capehart, T.W., Herbst, J.F., and Pinkerton, F.E. (1995) X-ray-absorption edge shifts in rare-earth-transition-metal compounds. Physical Review B, 52, 7907–7914.

Chaboy, J. (2009) Relationship between the structural distortion and the Mn electronic state in $La_{1-x}Ca_xMnO_3$: a Mn K-edge XANES study. Journal of Synchrotron Radiation, 16, 533–544.

Chalmin, E., Farges, F., and Brown, G.E. (2009) A pre-edge analysis of Mn K-edge XANES spectra to help determine the speciation of manganese in minerals and glasses. Contributions to Mineralogy and Petrology, 157, 111–126.

Cormie, A., Cross, A., Hollenkamp, A.F., and Donne, S.W. (2010) Cycle stability of birnessite manganese dioxide for electrochemical capacitors. Electrochimica Acta, 55, 7470–7478.

Cui, H., Liu, F., Feng, X.H., Tan, W., and Wang, M.K. (2010) Aging promotes todorokite formation from layered manganese oxide at near-surface conditions. Journal of Soils and Sediments, 10, 1540–1547.

Drits, V.A., Silvester, E., Gorshkov, A.I., and Manceau, A. (1997) The structure of synthetic monoclinic Na-rich birnessite and hexagonal birnessite. Part 1. Results from X-ray diffraction and selected area electron diffraction. American Mineralogist, 82, 946–961.

Farges, F. (2001) Crystal chemistry of iron in natural grandidierites: an X-ray

absorption fine-structure spectroscopy study. Physics and Chemistry of Minerals, 28, 619–629.
——— (2005) Ab initio and experimental pre-edge investigations of the Mn K-edge XANES in oxide-type materials. Physical Review B, 71, 155109.
Figueroa, S.J.A., Requejo, F.G., Lede, E.J., Lamaita, L., Peluso, M.A., and Sambeth, J.E. (2005) XANES study of electronic and structural nature of Mn-sites in manganese oxides with catalytic properties. Catalysis Today, 107, 849–855.
Frondel, C., Marvin, U.B., and Ito, J. (1960) Notes and News: New data on birnessite and hollandite. American Mineralogist, 45, 871–875.
Gaillot, A.C., Flot, D., Drits, V.A., Burghammer, M., Manceau, A., and Lanson, B. (2003) Structure of synthetic K-rich birnessites obtained by high-temperature decomposition of $KMnO_4$. I. Two-layer polytype from a 800°C experiment. Chemistry of Materials, 15, 4666–4678.
Gaillot, A.C., Drits, V.A., Plançon, A., and Lanson, B. (2004) Structure of synthetic K-rich birnessites obtained by high-temperature decomposition of $KMnO_4$. 2. Phase and structural heterogeneities. Chemistry of Materials, 16, 1890–1905.
Gaillot, A.C., Lanson, B., and Drits, V.A. (2005) Structure of birnessite obtained from decomposition of permanganate under soft hydrothermal conditions. 1. Chemical and structural evolution as a function of temperature. Chemistry of Materials, 17, 2959–2975.
Gaillot, A.C., Drits, V.A., Manceau, A., and Lanson, B. (2007) Structure of the synthetic K-rich phyllomanganate birnessite obtained by high-temperature decomposition of $KMnO_4$: Substructures of K-rich birnessite from 1000°C experiment. Microporous and Mesoporous Materials, 98, 267–282.
Galoisy, L., Calas, G., and Arrio, M.A. (2001) High-resolution XANES spectra of iron in minerals and glasses: structural information from the pre-edge region. Chemical Geology, 174, 307–319.
Garvie, L.A.J. and Craven, A.J. (1994a) Electron-beam-induced reduction of Mn^{4+} in manganese oxides as revealed by parallel EELS. Ultramicroscopy, 54, 83–92.
——— (1994b) High-resolution parallel electron energy-loss spectroscopy of Mn $L_{2,3}$-edges in inorganic manganese compounds. Physics and Chemistry of Minerals, 21, 191–206.
Gilbert, B., Frazer, B.H., Belz, A., Conrad, P.G., Nealson, K.H., Haskel, D., Lang, J.C., Srajer, G., and De Stasio, G. (2003) Multiple scattering calculations of bonding and X-ray absorption spectroscopy of manganese oxides. Journal of Physical Chemistry A, 17, 2839–2847.
Glatzel, P., Bergmann, U., Yano, J., Visser, H., Robblee, J.H., Gu, W.W., de Groot, F.M.F., Christou, G., Pecoraro, V.L., Cramer, S.P., and Yachandra, V.K. (2004) The electronic structure of Mn in oxides, coordination complexes, and the oxygen-evolving complex of photosystem II studied by resonant inelastic X-ray scattering. Journal of the American Chemical Society, 126, 9946–9959.
Grangeon, S. (2009) Cristallochimie des phyllomanganates nanocristallins désordonnés. Implications pour l'adsorption d'éléments métalliques. Ph.D. thesis, Université Joseph-Fourier, Grenoble I, France.
Grangeon, S., Lanson, B., Miyata, N., Tani, Y., and Manceau, A. (2010) Structure of nanocrystalline phyllomanganates produced by freshwater fungi. American Mineralogist, 95, 1608–1616.
Gunter, K.K., Miller, L.M., Aschner, M., Eliseev, R., Depuis, D., Gavin, C.E., and Gunter, T.E. (2002) XANES spectroscopy: A promising tool for toxicology: A tutorial. Neurotoxicology, 23, 127–146.
Gunter, T.E., Miller, L.M., Gavin, C.E., Eliseev, R., Salter, J., Buntinas, L., Alexandrov, A., Hammond, S., and Gunter, K.K. (2004) Determination of the oxidation states of manganese in brain, liver, and heart mitochondria. Journal of Neurochemistry, 88, 266–280.
Gunter, T.E., Gavin, C.E., Aschner, M., and Gunter, K.K. (2006) Speciation of manganese in cells and mitochondria: A search for the proximal cause of manganese neurotoxicity. Neurotoxicology, 27, 765–776.
Hopke, P.K. (1989) Target transformation factor analysis. Chemometrics and Intelligent Laboratory Systems, 6, 7–19.
Ito, A., Sato, Y., Sanada, T., Hatano, M., Horie, H., and Ohsawa, Y. (2011) In situ X-ray absorption spectroscopic study of Li-rich layered cathode material $Li[Ni_{0.17}Li_{0.2}Co_{0.07}Mn_{0.56}]O_2$. Journal of Power Sources, 196, 6828–6834.
Jokic, A., Frenkel, A.I., Vairavamurhty, M.A., and Huang, P.M. (2001) Birnessite catalysis of the Maillard reaction: Its significance in natural humification. Geophysical Research Letters, 28, 3899–3902.
Jürgensen, A., Widmeyer, J.R., Gordon, R.A., Bendell-Young, L.I., Moore, M.M., and Crozier, E.D. (2004) The structure of the manganese oxide on the sheath of the bacterium Leptothrix discophora: An XAFS study. American Mineralogist, 89, 1110–1118.
Kim, T.W., Yoo, H., Kim, I.Y., Ha, H.W., Han, A.R., Chang, J.S., Lee, J.S., and Hwang, S.J. (2001) A composite formation route to well-crystalline manganese oxide nanocrystals: High catalytic activity of manganate-alumina nanocomposites. Advanced Functional Materials, 21, 2301–2310.
Kraft, S., Stümpel, J., Becker, P., and Kuetgens, U. (1996) High resolution x-ray absorption spectroscopy with absolute energy calibration for the determination of absorption edge energies. Review of Scientific Instruments, 67, 681–687.
Kurata, H. and Colliex, C. (1993) Electron-energy-loss core-edge ctructures in manganese oxides. Physical Review B, 48, 2102–2108.
Laatikainen, K., Pakarinen, J., Laatikainen, M., Koivula, R., Harjula, R., and Paatero, E. (2010) Preparation of silica-supported nanoporous manganese oxides. Separation and Purification Technology, 75, 377–384.
Lafferty, B.J., Ginder-Vogel, M., Zhu, M.Q., Livi, K.J.T., and Sparks, D.L. (2010) Arsenite oxidation by a poorly crystalline manganese-oxide. 2. Results from X-ray absorption spectroscopy and X-ray diffraction. Environmental Science and Technology, 44, 8467–8472.
Lanson, B., Drits, V.A., Silvester, E.J., and Manceau, A. (2000) Structure of H-exchanged hexagonal birnessite and its mechanism of formation from Na-rich monoclinic buserite at low pH: New data from X-ray diffraction. American Mineralogist, 85, 826–835.
Lanson, B., Drits, V.A., Feng, Q., and Manceau, A. (2002) Crystal structure determination of synthetic Na-rich birnessite: Evidence for a triclinic one-layer cell. American Mineralogist, 87, 1662–1671.
Lingane, J.J. and Karplus, R. (1946) New method for determination of manganese. Industrial and Engineering Chemistry. Analytical Edition, 18, 191–194.
Loomer, D.B., Al, T.A., Weaver, L., and Cogswell, S. (2007) Manganese valence imaging in Mn minerals at the nanoscale using STEM-EELS. American Mineralogist, 92, 72–79.
Malinowski, E.R. (1977) Determination of the number of factors and the experimental error in a data matrix. Analytical Chemistry, 49, 612–617.
——— (1978) Theory of error for target factor analysis with applications to mass spectrometry and nuclear magnetic resonance spectrometry. Analytica Chimica Acta, 103, 339–354.
——— (1991) Factor Analysis in Chemistry. Wiley, New York.
Manceau, A. and Gallup, D.L. (2005) Nanometer-sized divalent manganese-hydrous silicate domains in geothermal brine precipitates. American Mineralogist, 90, 371–381.
Manceau, A., Gorshkov, A.I., and Drits, V.A. (1992) Structural chemistry of Mn, Fe, Co, and Ni in Mn hydrous oxides. I. Information from XANES spectroscopy. American Mineralogist, 77, 1133–1143.
Manceau, A., Marcus, M.A., and Tamura, N. (2002) Quantitative speciation of heavy metals in soils and sediments by synchrotron X-ray techniques. In P.A. Fenter, M.L. Rivers, N.C. Sturchio, and S.R. Sutton, Eds. Applications of Synchrotron Radiation in Low-Temperature Geochemistry and Environmental Science, 49, p. 341–428. Reviews in Mineralogy and Geochemistry, Mineralogical Society of America, Chantilly, Virginia.
Manceau, A., Tommaseo, C., Rihs, S., Geoffroy, N., Chateigner, D., Schlegel, M., Tisserand, D., Marcus, M.A., Tamura, N., and Chen, Z.S. (2005) Natural speciation of Mn, Ni and Zn at the micrometer scale in a clayey paddy soil using X-ray fluorescence, absorption, and diffraction. Geochimica et Cosmochimica Acta, 69, 4007–4034.
Mansot, J.L., Leone, P., Euzen, P., and Palvadeau, P. (1994) Valence of manganese, in a new oxybromide compound, determined by means of electron energy loss spectroscopy. Microscopy Microanalysis Microstructues, 5, 79–90.
Marcus, M.A., Westphal, A.J., and Fakra, S.C. (2008) Classification of Fe-bearing species from K-edge XANES data using two-parameter correlation plots. Journal of Synchrotron Radiation, 15, 463–468.
McKeown, D.A. and Post, J.E. (2001) Characterization of manganese oxide mineralogy in rock varnish and dendrites using X-ray absorption spectroscopy. American Mineralogist, 86, 701–713.
McKeown, D.A., Kot, W.K., Gan, H., and Pegg, I.L. (2003) X-ray absorption studies of manganese valence and local environment in borosilicate waste glasses. Journal of Non-Crystalline Solids, 328, 71–89.
Miyata, N., Tani, Y., Iwahori, K., and Soma, M. (2004) Enzymatic formation of manganese oxides by an *Acremonium*-like hyphomycete fungus, strain KR21-2. FEMS Microbiology Ecology, 47, 101–109.
Nakayama, M., Shamoto, M., and Kamimura, A. (2010) Surfactant-induced electrodeposition of layered manganese oxide with large interlayer space for catalytic oxidation of phenol. Chemistry of Materials, 22, 5887–5894.
Negra, C., Ross, D.S., and Lanzirotti, A. (2005) Oxidizing behavior of soil manganese: Interactions among abundance, oxidation state, and pH. Soil Science Society America Journal, 69, 87–95.
Pecher, K., McCubbery, D., Kneedler, E., Rothe, J., Bargar, J., Meigs, G., Cox, L., Nealson, K., and Tonner, B. (2003) Quantitative charge state analysis of manganese biominerals in aqueous suspension using Scanning Transmission X-ray Microscopy (STXM). Geochimica et Cosmochimica Acta, 67, 1089–1098.
Petit, P.E., Farges, F., Wilke, M., and Sole, V.A. (2001) Determination of the iron oxidation state in Earth materials using XANES pre-edge information. Journal of Synchrotron Radiation, 8, 952–954.
Pinaud, B.A., Chen, Z.B., Abram, D.N., and Jaramillo, T.F. (2011) Thin films of sodium birnessite-type MnO(2): Optical properties, electronic band structure, and solar photoelectrochemistry. Journal of Physical Chemistry C, 115, 11830–11838.
Post, J.E., Heaney, P.J., and Hanson, J. (2003) Synchrotron X-ray diffraction of the structure and dehydration behavior of todorokite. American Mineralogist, 88, 142–150.
Ramallo-Lopez, J.M., Lede, E.J., Requejo, F.G., Rodriguez, J.A., Kim, J.Y., Rosas-

Salas, R., and Dominguez, J.M. (2004) XANES characterization of extremely nanosized metal-carbonyl subspecies (Me) Cr, Mn, Fe, and Co) confined into the mesopores of MCM-41 materials. Journal of Physical Chemistry B, 108, 20005–20010.

Ressler, T., Brock, S.L., Wong, J., and Suib, S.L. (1999) Multiple-scattering EXAFS analysis of tetraalkylammonium manganese oxide colloids. Journal of Physical Chemistry, 103, 6407–6420.

Ressler, T., Wong, J., Roos, J., and Smith, I. (2000) Quantitative speciation of Mn-bearing particulates emitted from autos burning (methylcyclopentadienyl) manganese tricarbonyl-added gasolines using XANES spectroscopy. Environmental Science and Technology, 34, 950–958.

Riedl, T., Gemming, T., and Wetzig, K. (2006) Extraction of EELS white-line intensities of manganese compounds: Methods, accuracy, and valence sensitivity. Ultramicroscopy, 106, 284–291.

Rumble, C., Conry, T.E., Doeff, M., Cairns, E.J., Penner-Hahn, J.E., and Deba, A. (2010) Structural and electrochemical investigation of $Li(Ni_{0.4}Co_{0.15}Al_{0.05}Mn_{0.4})O_2$ cathode material. Journal of the Electrochemical Society, 157, A1317–A1322.

Saratovsky, I., Wightman, P.G., Pasten, P.A., Gaillard, J.F., and Poeppelmeier, K.R. (2006) Manganese oxides: Parallels between abiotic and biotic structures. Journal of the American Chemical Society, 128, 11188–11198.

Silvester, E., Manceau, A., and Drits, V.A. (1997) The structure of synthetic monoclinic Na-rich birnessite and hexagonal birnessite. Part 2. Results from chemical studies and EXAFS spectroscopy. American Mineralogist, 82, 962–978.

Tang, X.H., Li, H.J., Liu, Z.H., Yang, Z.P., and Wang, Z.L. (2010) Preparation and capacitive property of manganese oxide nanobelt bundles with birnessite-type structure. Journal of Power Sources, 196, 855–859.

Thackeray, M.M. (1997) Manganese oxides for lithium batteries. Progress in Solid State Chemistry, 25, 1–71.

Toupin, M., Brousse, T., and Belanger, D. (2004) Charge storage mechanism of MnO_2 electrode used in aqueous electrochemical capacitor. Chemistry of Materials, 16, 3184–3190.

Vetter, K.J. and Jaeger, N. (1966) Potentialausbildung an der Mangan-dioxid-elektrode als Oxidelektrode mit nichtstöchiometrischem Oxid. Electrochimica Acta, 11, 401–419.

Villalobos, M., Toner, B., Bargar, J., and Sposito, G. (2003) Characterization of the manganese oxide produced by *Pseudomonas putida* strain MnB1. Geochimica et Cosmochimica Acta, 67, 2649–2662.

Wang, H., Hamanaka, S., Yokoyama, T., Yoshikawa, H., and Awaga, K. (2011) In-situ XAFS studies of Mn12 molecular-cluster batteries: Super-reduced Mn12 clusters in solid-state electrochemistry. Chemistry—An Asian Journal, 6, 1074–1079.

Wang, L.Z., Ebina, Y., Takada, K., and Sasaki, T. (2004) Ultrathin hollow nanoshells of manganese oxide. Chemical Communication, 9, 1074–1075.

Wang, L.Z., Sakai, N., Ebina, Y., and Sasaki, T. (2005) Inorganic multilayer films of manganese oxide nanosheets and aluminum polyoxocations: Fabrication, structure, and electrochemical behavior. Chemistry of Materials, 17, 1352–1357.

Wasserman, S.R., Allen, P.G., Shuh, D.K., Bucher, J.J., and Edelstein, N.M. (1999) EXAFS and principal component analysis: a new shell game. Journal of Synchrotron Radiation, 6, 284–286.

Webb, S.M., Dick, G.J., Bargar, J.R., and Tebo, B.M. (2005) Evidence for the presence of Mn(III) intermediates in the bacterial oxidation of Mn(II). Proceedings of the National Academy of Sciences, 102, 558–5563.

Weiner, P.H., Malinowski, E.R., and Levinston, A.R. (1970) Factor analysis of solvent shifts in proton magnetic resonance. Journal of Physical Chemistry, 74, 4537–4542.

Wilke, M., Farges, F., Partzsch, G.M., Schmidt, C., and Behrens, H. (2001) Speciation of Fe in silicate glasses and melts by in-situ XANES spectroscopy. American Mineralogist, 92, 44–56.

Wong, J., Lytle, F.W., Messmer, R.P., and Maylotte, D.H. (1984) K-edge absorption spectra of selected vanadium compounds. Physical Review B, 30, 5596–5610.

Yan, J., Fan, Z.J., Wei, T., Qian, W.Z., Zhang, M.L., and Wei, F. (2010) Fast and reversible surface redox reaction of grapheme-MnO_2 composites as supercapacitor electrodes. Carbon, 48, 3825–3833.

Yan, W.B., Ayvazian, T., Kim, J., Liu, Y., Donavan, K.C., Xing, W.D., Yang, Y.G., Hemminger, J.C., and Penner, R.M. (2011) Mesoporous manganese oxide nanowires for high-capacity, high-rate, hybrid electrical energy storage. ACS Nano, 5, 8275–8287.

Zhang, S.L., Livi, K.J.T., Gaillot, A.C., Stone, A.T., and Veblen, D.R. (2010) Determination of manganese valence states in (Mn^{3+}, Mn^{4+}) minerals by electron energy-loss spectroscopy. American Mineralogist, 95, 1741–1746.

Manuscript received June 4, 2011
Manuscript accepted February 5, 2012
Manuscript handled by Pupa Gilbert

Supplementary materials for the article

Determination of Mn Valence States in Mixed-Valent Manganates by XANES Spectroscopy

ALAIN MANCEAU,[1] MATTHEW A. MARCUS,[2] AND SYLVAIN GRANGEON[1]

[1]ISTerre, CNRS and Université de Grenoble 1, F-38041 Grenoble Cedex 9, France.

[2]Advanced Light Source, Lawrence Berkeley National Laboratory, One Cyclotron Road, Berkeley, CA 94720, USA

Pre-edge Background Subtraction and Post-edge Normalization

The usual procedure for subtracting a pre-edge linear background from XANES or EXAFS data involves choosing a line or polynomial which passes through the data at the lowest energies. However, the rise of the edge (or pre-edge) has a tail which extends far into the pre-edge region. What is often done, then, is to estimate "by eye" what that tail looks like and to subtract a pre-edge line which fits under it with the exclusion of the tail. Instead, both the tail and a linear pre-edge were fitted as:

$$y(E) = \frac{a}{E_0 - E} + b + c(E - E_0)$$

where E_0, a, b, and c are parameters, and the fit is done over a user-selected range which generally comes up half or a third of the way up the first pre-edge rise (Fig. S1). The linear term was then subtracted as the pre-edge background. In fluorescence data for which the elastic contribution "leaks" into the fluorescence channel below the edge, another term was added:

$$y(E) = \frac{a}{E_0 - E} + b + c(E - E_0) + \frac{d}{(E - E_f)^4}$$

to approximate the upward curve generated by the elastic contribution being picked up by the tail of the detector response. In this case, E_f is the center of the detector passband. This extra term was not used for electron-yield data, which constitutes most of the database.

After pre-edge subtraction, a line was fitted through the data ranging from an energy of about 6600eV to the end of the data, chosen "by eye" so that the resulting normalized data (pre-edge subtracted divided by post-edge line) oscillates around one. The undoubted subjectivity of this procedure was mitigated in the Combo fits by allowing a slope as a free parameter. To do this, the weighted sum of chosen references was multiplied by a term $1 + \alpha(E - E_1)$ where α is a free parameter and E_1 is the energy for the start of data. This procedure largely compensates for the arbitrariness of the post-edge slope.

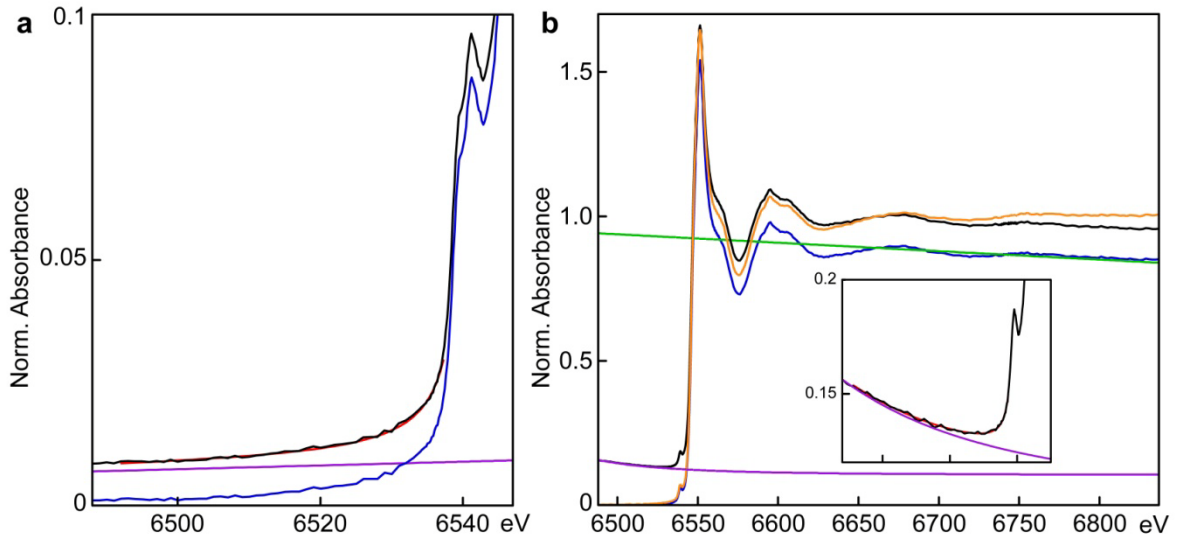

Figure S1. (a) Pre-edge normalization illustrated for a typical electron-yield data. (b) Pre- and post-edge normalization for a typical fluorescence data. Black: raw data, red: fit to pre-edge plus edge rise, purple: pre-edge line to be subtracted, blue: pre-edge normalized spectrum, green: post-edge line, orange: final pre- and post-edge normalized spectrum.

Principal Component Analysis

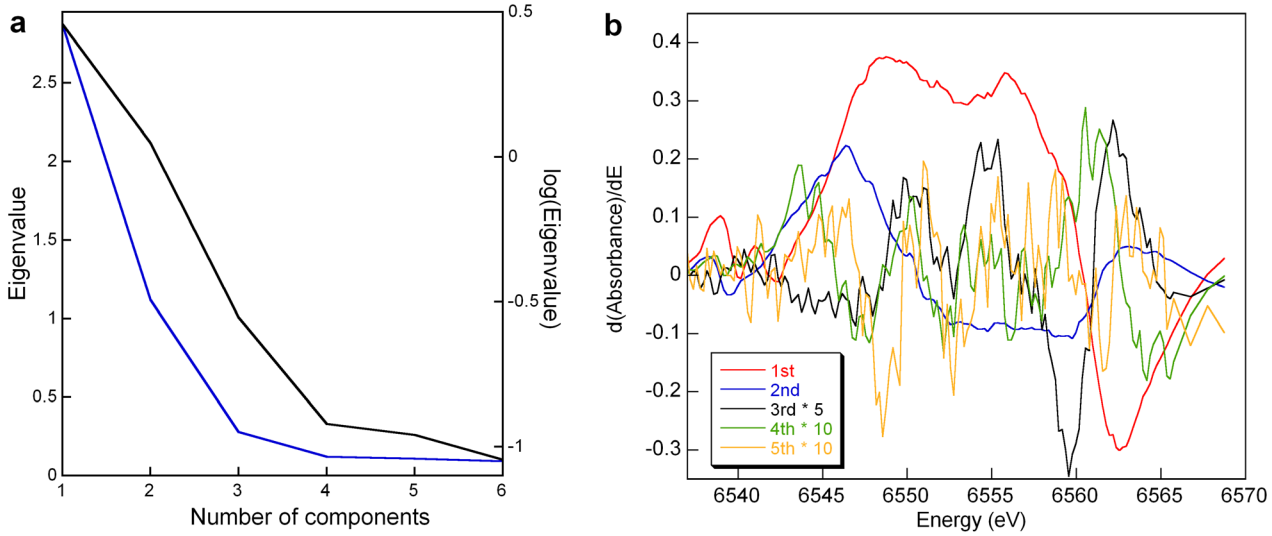

Figure S2. (a) Decline of the eigenvalues (λ) from the PCA in the 6535-6570 eV interval of the XANES derivatives for the twelve mixed-valent tectomanganates and phyllomanganates with no or little layer Mn^{3+}. (b) First five principal components weighted by eigenvalues (λ). For clarity, the amplitudes of the 3rd, 4th, and 5th components have been multiplied by 5, 10, and 10, respectively. PCA identifies three orthogonal components.

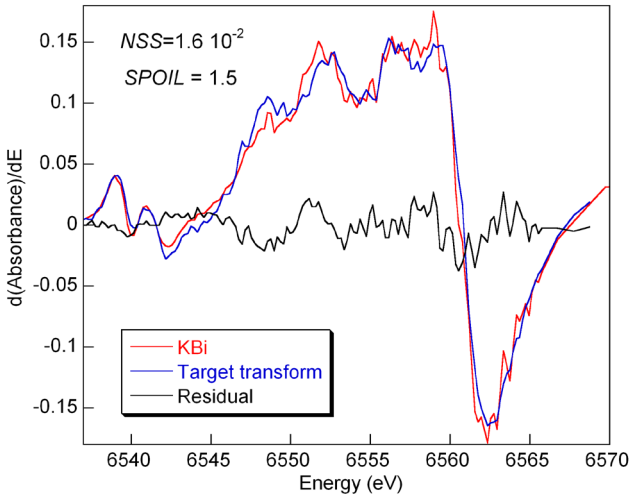

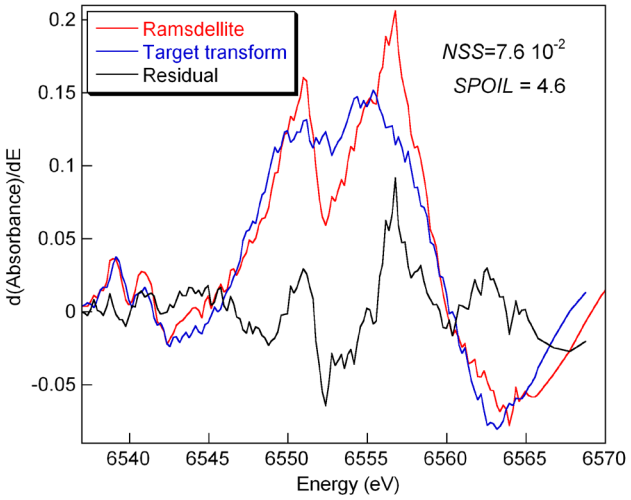

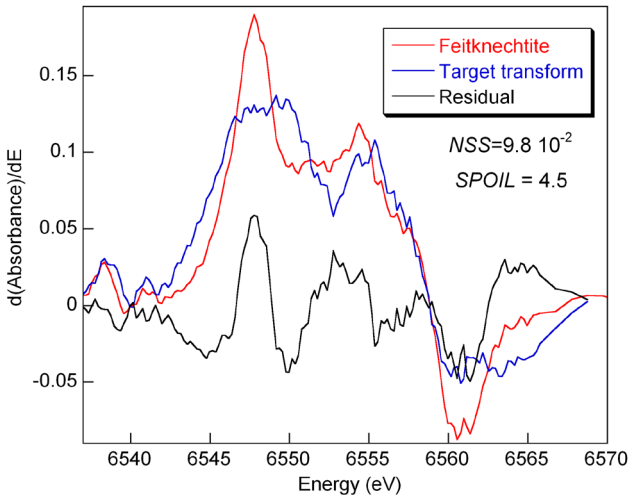

Figure S3. Target transforms of two Mn^{4+} (KBi, ramsdellite) and one Mn^{3+} (feitknechtite) references with three principal components.

The Combo Method

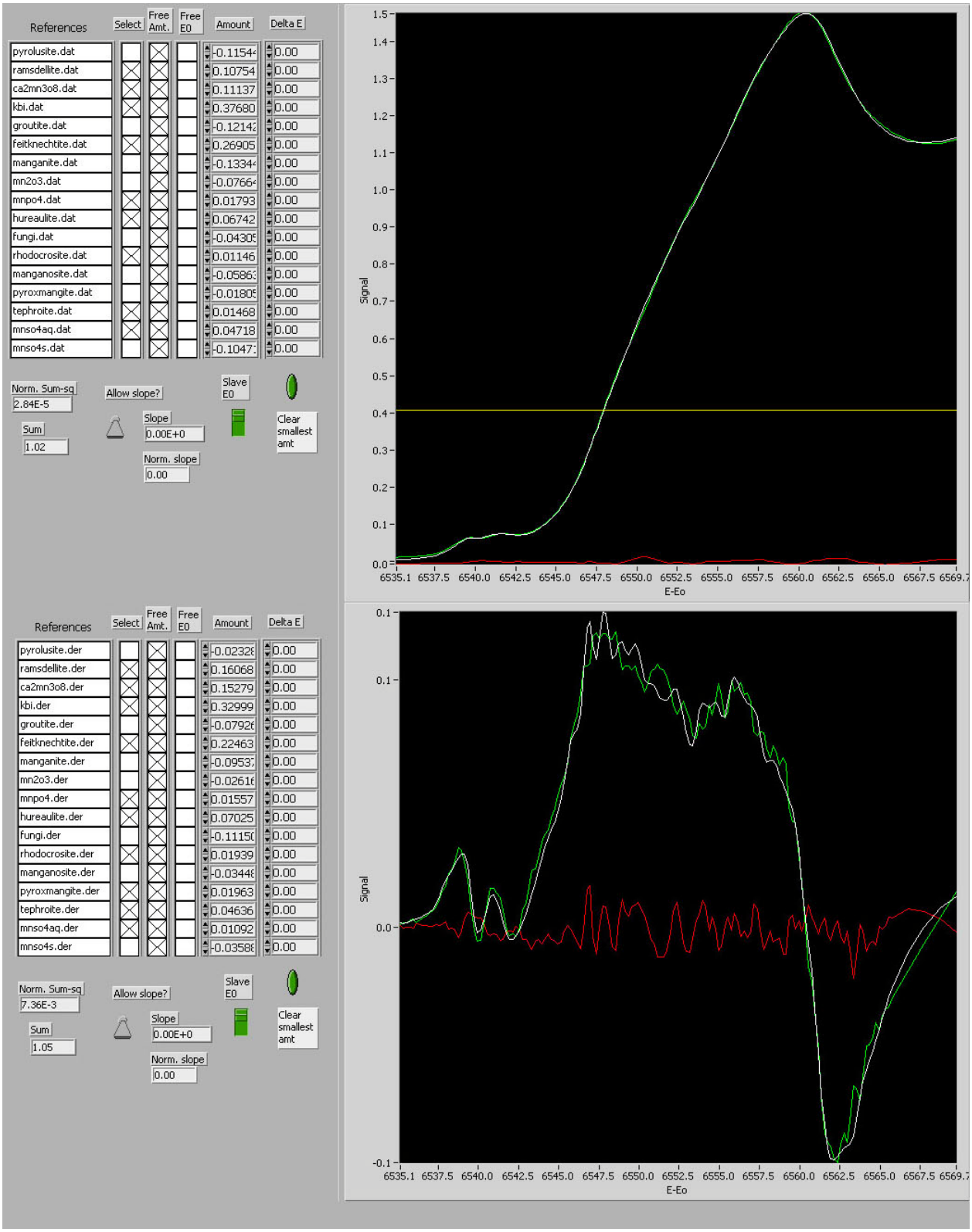

Figure S4. Linear combination fits of the XANES and derivative spectra for KR21-2 with the Combo method and the "Linear Fit w overabsorption" software from beamline 10.3.2 at the Advanced Light Source (http://xraysweb.lbl.gov/uxas/index.htm).

Error bars on individual components in a Combo fit are irrelevant, since that is not what we are after. Further, the error will be highly correlated in that one can push on one component and pull on a couple of others and come up with almost the same fit. Thus, the only obvious way to evaluate the error inherent in the method is to try it out on as many known mixed-valent compounds as possible and see how well it works. Normal statistical methods do not really apply because they assume that the error comes from noise in the unknown data, rather than from an incomplete model.

Table S1. Results from the PCA of the derivatives for the twelve mixed-valent tectomanganates and phyllomanganates with no or little layer Mn^{3+} in the 6535-6570 eV interval.

PC[a]	Eigenvalue[b]	% of variance[c]	*IND* x 10^{3}[d]	*NSS*-Tot	% of variation[f]
1	2.87	85.8	2.93	0.14	-
2	1.12	13.1	1.14	$1.3\ 10^{-2}$	91
3	0.28	0.8	0.94	$5.4\ 10^{-3}$	58
4	0.12	0.1	1.07	$3.9\ 10^{-3}$	28
5	0.11	<0.1	1.23	$2.6\ 10^{-3}$	33
6	0.09	<0.1	1.53	$1.9\ 10^{-3}$	27

[a] Principal component number (*C*). [b] Values of the diagonal matrix in the PCA after consecutive elimination of the components. Eigenvalues rank PCs according to their importance to reproduce data. [c] Fraction of the derivative signal accounted for by the first *N* components out of a maximum of six:

$f_c \equiv \left\|\vec{Y}^C\right\| / \left\|\vec{Y}\right\| = \sum_{c=1}^{6} \Lambda_c^2 / \sum_{c=1}^{N} \Lambda_c^2$. [d] Malinowski (1977) indicator value. [e] Normalized sum-squared total = $\sum_{spectra}\sum_{n}[\text{data} - \text{fit}]^2 / \sum_{spectra}\sum_{n}[\text{data}]^2$. This parameter is the normalized sum-squared (*NSS*) residual of the entire set of data, taken as one. [f] Marginal variation of *NNS-Tot* = $[(NSS\text{-}Tot)_{i+1}\text{-}(NSS\text{-}Tot)_i]/(NSS\text{-}Tot)_{i+1}$.

Table S2. Results from target transformation and weight fractions of the pure-valence references from the Combo fit of XANES spectra and derivatives in the 6535-6570 eV interval.

XANES	**REF4-1**	**REF4-2**	**REF4-3**	**REF4-4**	**Sum**	**REF3-1**	**REF3-2**	**REF3-3**	**REF3-4**	**REF3-5**	**Sum**	**REF2-1**	**REF2-2**	**REF2-3**	**REF2-4**	**REF2-5**	**REF2-6**	**REF2-7**	**REF2-8**	**Sum**	**Sum**	***NSS* x 10^5**
Hollandite		0.493	0.123	0.204	0.820	0.035	0.024		0.135		0.194									0.00	0.99	8.28
Psilomelane		0.222	0.143	0.382	0.747		0.149			0.089	0.238									0.00	0.99	10.20
Todorokite_Japan		0.443	0.143	0.193	0.779		0.081		0.151		0.232									0.00	1.01	15.00
Todorokite_SAF		0.191	0.090	0.416	0.697		0.169		0.053	0.074	0.296									0.00	0.99	15.50
KBi8		0.113	0.029	0.688	0.830		0.108			0.052	0.160									0.00	0.99	1.17
HBi5		0.230	0.092	0.346	0.668		0.280			0.011	0.291							0.049		0.049	1.01	4.35
KR21-2		0.107	0.111	0.377	0.595		0.269			0.018	0.287	0.067		0.011			0.015	0.047		0.140	1.02	2.84
KR21-Cu-A		0.189	0.169	0.392	0.750		0.114			0.045	0.159			0.010		0.005		0.069		0.084	0.99	3.50
KR21-Cu-B				0.058	0.058		0.509		0.102		0.611		0.084	0.052		0.192				0.328	1.00	19.80
SP6-Cu-A	0.020	0.054	0.173	0.464	0.711			0.091	0.036		0.127			0.030		0.088	0.006	0.034		0.158	1.00	5.99
SP6-Cu-B	0.046			0.063	0.109		0.355		0.162		0.517		0.049	0.050		0.248				0.347	0.97	15.20
SP6-Cu-C				0.026	0.026		0.116		0.269		0.385		0.035	0.131		0.415				0.581	0.99	29.9
1st derivative	**REF4-1**	**REF4-2**	**REF4-3**	**REF4-4**	**Sum**	**REF3-1**	**REF3-2**	**REF3-3**	**REF3-4**	**REF3-5**	**Sum**	**REF2-1**	**REF2-2**	**REF2-3**	**REF2-4**	**REF2-5**	**REF2-6**	**REF2-7**	**REF2-8**	**Sum**	**Sum**	***NSS* x 10^3**
SPOIL	6.0	4.6	13.1	1.5		9.4	4.5	7.2	5.0	10.3		5.4	4.7	5.0	13.0	7.3	7.8	5.5	5.4			
***NSS* x 10**	1.9	0.8	1.6	0.2		2.1	1.0	1.3	2.3	3.6		1.1	1.1	3.3	5.6	1.9	2.5	1.6	1.4			
Hollandite		0.561	0.194	0.106	0.861	0.092			0.076		0.168					0.017				0.017	1.05	14.90
Psilomelane		0.317	0.221	0.289	0.827		0.086			0.074	0.160				0.002	0.017	0.018			0.037	1.02	16.50
Todorokite_Japan		0.528	0.192	0.097	0.817	0.107		0.036	0.080		0.223					0.006				0.006	1.05	16.50
Todorokite_SAF		0.278	0.190	0.308	0.776		0.135			0.099	0.234					0.021	0.009			0.030	1.04	18.80
KBi8		0.120	0.076	0.652	0.848		0.102			0.042	0.144			0.005			0.007			0.012	1.00	4.04
HBi5		0.287	0.137	0.292	0.716		0.221			0.030	0.251	0.004		0.016		0.024	0.030			0.074	1.04	10.20
KR21-2		0.161	0.153	0.330	0.644		0.225			0.016	0.241	0.070		0.019		0.020	0.046	0.011		0.166	1.05	7.36
KR21-Cu-A		0.228	0.184	0.374	0.786		0.066			0.052	0.118	0.036		0.014		0.013	0.035	0.011		0.109	1.01	7.95
KR21-Cu-B	0.081		0.048	0.032	0.161		0.443		0.051		0.494	0.127	0.115	0.021	0.014	0.079				0.356	1.01	11.60
SP6-Cu-A	0.044	0.097	0.270	0.374	0.785		0.056				0.056	0.006		0.031		0.045	0.018	0.072		0.172	1.01	12.10
SP6-Cu-B	0.091		0.105		0.196		0.380	0.002	0.027		0.409	0.112	0.142	0.009	0.034	0.060	0.007			0.364	0.97	12.90
SP6-Cu-C	0.008		0.069		0.077		0.189		0.129		0.318	0.128	0.162	0.088	0.036	0.117	0.036			0.567	0.96	22.30

NSS is the normalized sum-squared residual = $\sum_n[\text{data} - \text{fit}]^2 / \sum_n[\text{data}]^2$.

Table S3. Results from target transformation and weight fractions of the pure-valence references from the Combo fit of XANES spectra and derivatives in the 6521-6653 eV interval

XANES	**REF4-1**	**REF4-2**	**REF4-3**	**REF4-4**	**Sum**	**REF3-1**	**REF3-2**	**REF3-3**	**REF3-4**	**REF3-5**	**Sum**	**REF2-1**	**REF2-2**	**REF2-3**	**REF2-4**	**REF2-5**	**REF2-6**	**REF2-7**	**Sum**	**Sum**	***NSS* x 10^5**	**Slope x 10^4**
Hollandite		0.493	0.093	0.230	0.816	0.031	0.018		0.149		0.198								0.000	1.01	7.40	-1.23
Psilomelane		0.251	0.158	0.354	0.763	0.123	0.046			0.056	0.225						0.003		0.003	0.99	8.95	1.67
Todorokite_Japan		0.442	0.130	0.208	0.780	0.002	0.079		0.150		0.231								0.000	1.01	11.80	-0.74
Todorokite_SAF		0.183	0.133	0.388	0.704	0.027	0.183			0.079	0.289								0.000	0.99	11.90	1.29
KBi8		0.136	0.034	0.669	0.839	0.068	0.017	0.034		0.036	0.155			0.002					0.002	1.00	1.93	0.66
HBi5		0.217	0.064	0.366	0.647		0.281		0.010	0.024	0.315		0.010					0.034	0.044	1.01	3.98	-0.70
KR21-2		0.131	0.157	0.339	0.627		0.256			0.007	0.263	0.041		0.010				0.091	0.142	1.03	3.00	-2.73
KR21-Cu-A		0.208	0.190	0.366	0.764	0.052	0.069			0.023	0.144			0.008				0.079	0.087	1.00	3.63	1.34
KR21-Cu-B				0.068	0.068		0.500		0.098		0.598		0.094	0.048		0.190			0.332	1.00	13.80	0.34
SP6-Cu-A		0.088	0.167	0.481	0.736		0.084		0.007		0.091			0.015		0.106		0.048	0.169	1.00	5.29	0.74
SP6-Cu-B	0.069		0.064		0.133		0.247	0.130	0.100		0.477	0.033		0.052	0.019	0.240		0.022	0.366	0.98	19.90	2.70
SP6-Cu-C				0.064	0.064		0.132		0.191		0.323	0.039		0.099		0.467			0.605	0.99	23.60	0.83
1st derivative	**REF4-1**	**REF4-2**	**REF4-3**	**REF4-4**	**Sum**	**REF3-1**	**REF3-2**	**REF3-3**	**REF3-4**	**REF3-5**	**Sum**	**REF2-1**	**REF2-2**	**REF2-3**	**REF2-4**	**REF2-5**	**REF2-6**	**REF2-7**	**Sum**	**Sum**	***NSS* x 10^3**	
Hollandite		0.559	0.193	0.108	0.860	0.092			0.076		0.168					0.017			0.017	1.05	15.20	
Psilomelane		0.309	0.220	0.293	0.822		0.091			0.075	0.166					0.017	0.019		0.036	1.02	17.20	
Todorokite_Japan		0.526	0.193	0.097	0.816	0.108		0.035	0.079		0.222					0.005			0.005	1.04	17.30	
Todorokite_SAF		0.274	0.192	0.309	0.775		0.139			0.096	0.235					0.020	0.009		0.029	1.04	19.20	
KBi8		0.124	0.079	0.649	0.852		0.101			0.038	0.139			0.006	0.004		0.004		0.014	1.01	4.25	
HBi5		0.282	0.135	0.295	0.712		0.222			0.032	0.254	0.005		0.016		0.025	0.028		0.074	1.04	10.50	
KR21-2		0.158	0.152	0.331	0.641		0.225			0.017	0.242	0.070		0.019		0.020	0.044	0.013	0.166	1.05	7.50	
KR21-Cu-A		0.224	0.183	0.376	0.783		0.068			0.053	0.121	0.035		0.014		0.014	0.033	0.013	0.109	1.01	8.30	
KR21-Cu-B	0.080		0.047	0.033	0.160		0.442		0.052		0.494	0.127	0.115	0.021	0.013	0.079			0.355	1.01	11.80	
SP6-Cu-A	0.042	0.097	0.266	0.377	0.782		0.057				0.057	0.007		0.030		0.046	0.016	0.072	0.171	1.01	13.10	
SP6-Cu-B	0.090		0.104		0.194		0.381		0.028		0.409	0.111	0.143	0.010	0.033	0.059	0.008		0.364	0.97	13.70	
SP6-Cu-C	0.010		0.070		0.080		0.189		0.125		0.314	0.131	0.160	0.088	0.036	0.118	0.036		0.569	0.96	23.00	

Table S4. Fractional and average valence states of Mn obtained from the Combo fit of XANES spectra and derivatives in the 6521-6653 eV interval.

	Fractional Mn^{4+}		Fractional Mn^{3+}		Fractional Mn^{2+}		Average Mn valence	
	XANES	Structure	XANES	Structure	XANES	Structure	XANES	Structure/Titration
XANES								
Hollandite	0.80	-	0.20	-	-	-	3.80	3.75-3.83
Psilomelane	0.77	-	0.23	-	-	-	3.77	3.75-3.75
Todorokite_Japan	0.77	-	0.23	-	-	-	3.77	3.72-3.73
Todorokite_SAF	0.71	0.73	0.29	0.27	-	-	3.71	3.73
KBi8	0.84	0.92	0.16	0.08	-	-	3.84	3.87-3.92
HBi5	0.64	0.72	0.31	0.22	0.04	0.05	3.60	3.66
KR21-2	0.61	-	0.25	-	0.14	-	3.47	-
KR21-Cu-A	0.77		0.14		0.09		3.68	
KR21-Cu-B	0.07		0.60		0.33		2.74	
SP6-Cu-A	0.74		0.09		0.17		3.57	
SP6-Cu-B	0.14		0.49		0.38		2.76	
SP6-Cu-C	0.06		0.33		0.61		2.45	
1^{st} derivative								
Hollandite	0.82	-	0.16	-	0.02	-	3.81	3.75-3.83
Psilomelane	0.80	-	0.16	-	0.04	-	3.77	3.75-3.75
Todorokite_Japan	0.78	-	0.21	-	-	-	3.78	3.72-3.73
Todorokite_SAF	0.75	0.73	0.23	0.27	0.03	-	3.72	3.73
KBi8	0.85	0.92	0.14	0.08	0.01	-	3.83	3.87-3.92
HBi5	0.68	0.72	0.24	0.22	0.07	0.05	3.61	3.66
KR21-2	0.61	-	0.23	-	0.16	-	3.45	-
KR21-Cu-A	0.77		0.12		0.11		3.67	
KR21-Cu-B	0.16		0.49		0.35		2.81	
SP6-Cu-A	0.77		0.06		0.17		3.60	
SP6-Cu-B	0.20		0.42		0.38		2.82	
SP6-Cu-C	0.08		0.33		0.59		2.49	

Table S5. Average valence states of Mn derived from the Combo method and the integration method proposed by Capehart et al. (1995). Values in bold denote the best agreement with titration/structure among the three methods.

	Structure/Titration	Combo[a]	Capehart[b]	Capehart[c]
Hollandite	3.75-3.83	**3.81**	3.69	3.69
Psilomelane	3.75-3.75	**3.76**	3.68	3.68
Todorokite_Japan	3.72-3.73	**3.77**	3.66	3.66
Todorokite_SAF	3.73	**3.70**	3.66	3.66
KBi8	3.87-3.92	**3.84**	3.72	3.72
HBi5	3.66	**3.61**	3.53	3.53
KR21-2	-	3.45	3.34	3.32
KBi10	3.67-3.75	**3.69**	3.63	3.63
TcBi	3.69	3.81	**3.66**	**3.66**
Lithiophorite	3.67-3.68	3.55	3.55	3.55
Hausmannite	2.67	2.76	2.73	**2.66**

[a] Least-squares fit of the main edge in the 6535-6570 eV interval; [b] Calibration curve obtained with all pure valence Mn species: $v = 1.816 + 0.275 \times \Delta E$; [c] Calibration curve obtained with MnO, Mn_2O_3 and MnO_2 (pyrolusite): $v = 1.687 + 0.295 \times \Delta E$.

References

Capehart, T.W., Herbst, J.F., and Pinkerton, F.E. (1995) X-ray-absorption edge shifts in rare-earth-transition-metal compounds. Physical Review, B52, 7907-7914.

Malinowski, E.R. (1977) Determination of the number of factors and the experimental error in a data matrix. Analytical Chemistry, 49, 612-617.